

# Incorporating Network Scale River Bathymetry to Improve Characterization of Fluvial Processes in Flood Modeling

Sayan Dey<sup>1</sup>, Siddharth Saksena<sup>2</sup>, Danielle Winter<sup>1</sup>, Venkatesh Mohan Merwade<sup>1</sup>, and Sara K McMillan<sup>1</sup>

<sup>1</sup>Purdue University

<sup>2</sup>Virginia Tech

November 30, 2022

## Abstract

Several studies have focused on the importance of river bathymetry (channel geometry) in hydrodynamic routing along individual reaches. However, its effect on other watershed processes such as infiltration and surface water (SW) – groundwater (GW) interactions has not been explored across large river networks. Surface and subsurface processes are interdependent, therefore, errors due to inaccurate representation of one watershed process can cascade across other hydraulic or hydrologic processes. This study hypothesizes that accurate bathymetric representation is not only essential for simulating channel hydrodynamics but also affects subsurface processes by impacting SW-GW interactions. Moreover, quantifying the effect of bathymetry on surface and subsurface hydrological processes across a river network can facilitate an improved understanding of how bathymetric characteristics affect these processes across large spatial domains. The study tests this hypothesis by developing physically-based distributed models capable of bidirectional coupling (SW-GW) with four configurations with progressively reduced levels of bathymetric representation. A comparison of hydrologic and hydrodynamic outputs shows that changes in channel geometry across the four configurations has a considerable effect on infiltration, lateral seepage, and location of water table across the entire river network. In addition, the results from this study provide insights into the level of bathymetric detail required for accurately simulating flooding-related physical processes while also highlighting potential issues with ignoring bathymetry across lower order streams such as spurious backwater flow, inaccurate water table elevations, and incorrect inundation extents.



18 **Abstract**

19         Several studies have focused on the importance of river bathymetry (channel geometry) in  
20 hydrodynamic routing along individual reaches. However, its effect on other watershed processes  
21 such as infiltration and surface water (SW) – groundwater (GW) interactions has not been explored  
22 across large river networks. Surface and subsurface processes are interdependent, therefore, errors  
23 due to inaccurate representation of one watershed process can cascade across other hydraulic or  
24 hydrologic processes. This study hypothesizes that accurate bathymetric representation is not only  
25 essential for simulating channel hydrodynamics but also affects subsurface processes by impacting  
26 SW-GW interactions. Moreover, quantifying the effect of bathymetry on surface and subsurface  
27 hydrological processes across a river network can facilitate an improved understanding of how  
28 bathymetric characteristics affect these processes across large spatial domains. The study tests this  
29 hypothesis by developing physically-based distributed models capable of bidirectional coupling  
30 (SW-GW) with four configurations with progressively reduced levels of bathymetric  
31 representation. A comparison of hydrologic and hydrodynamic outputs shows that changes in  
32 channel geometry across the four configurations has a considerable effect on infiltration, lateral  
33 seepage, and location of water table across the entire river network. In addition, the results from  
34 this study provide insights into the level of bathymetric detail required for accurately simulating  
35 flooding-related physical processes while also highlighting potential issues with ignoring  
36 bathymetry across lower order streams such as spurious backwater flow, inaccurate water table  
37 elevations, and incorrect inundation extents.

## 38 **1 Introduction**

39 River bathymetry is critical for simulating fluvial hydrodynamics accurately in flood  
40 inundation mapping. Several studies have investigated the impact of poor bathymetric  
41 representation on one- and two-dimensional flow models and concluded that river bathymetry  
42 affects hydraulic attributes significantly. Specifically, inaccurate estimation of channel storage  
43 capacity may lead to errors in predicting the depth and extent of inundation. Similarly, errors in  
44 estimating longitudinal slope affect the magnitude of streamflow and erroneous thalweg  
45 representation can contribute to poor estimation of shear and velocity (Cook and Merwade, 2009;  
46 Dey, 2016; Dey et al., 2019; Grimaldi et al., 2018; Saleh et al., 2012). However, these studies have  
47 only focused on the influence of river bathymetry on hydrodynamic simulations, usually along a  
48 single reach, and not the entire river network. The hydrodynamic models implemented by these  
49 studies ignore within reach hydrologic processes and route the flood wave along the river channel  
50 using known surface boundary conditions such as flow or stage hydrographs derived from gauges  
51 or estimated from loosely coupled hydrologic model.

52 Fluvial systems involve a complex interplay between various hydrologic and hydraulic  
53 processes such as rainfall-generated surface runoff, infiltration and surface water – groundwater  
54 (SW-GW) interactions, in addition to hydrodynamic flow regimes along river channels.  
55 (Fleckenstein et al., 2010; Kollet and Maxwell, 2008; Saksena and Merwade, 2017a; Stewart et  
56 al., 1999). Several studies have shown that stream-aquifer interactions are sensitive to WSE  
57 fluctuations in the river (Flipo et al., 2014; Tran et al., 2020; Vergnes and Habets, 2018). The water  
58 table (GWT) at the floodplains is highly correlated with the WSE in the river (Claxton et al., 2003;  
59 Jung et al., 2004). Coupled with the fact that river geometry is one of the most important factors  
60 affecting WSE, errors in WSE estimation can propagate to these hydrologic processes. Therefore,

61 the inadequate topographic representation that results from excluding river bathymetry can  
62 influence how surface and subsurface processes interact with each other in a simulation model  
63 (Cardenas and Jiang, 2010; Wörman et al., 2006). The cascading effects of inaccurate bathymetric  
64 representation are obscured to some degree in loosely coupled hydrologic and hydrodynamic  
65 (H&H) models traditionally implemented in large-scale flood modeling applications because the  
66 upstream boundary conditions and lateral inflows for simulating river hydrodynamics are  
67 estimated separately using hydrologic models with simplistic surface routing (Baratelli et al., 2016;  
68 Follum et al., 2020; Rajib et al., 2020; Saleh et al., 2012; Vergnes and Habets, 2018). Loose  
69 coupling enables hydrologic fluxes such as discharge to move from land surface to river but  
70 ignores potential feedbacks such as backwater effects and hyporheic exchanges which might be  
71 exacerbated by the lack of river bathymetry, especially at large watershed scales (Brunner et al.,  
72 2017; Käser et al., 2014; Mejia and Reed, 2011).

73         There is an increasing interest in developing high-resolution flood models spanning  
74 regional or continental scales, owing to considerable advances in H&H model capabilities and data  
75 acquisition techniques (Altenau et al., 2017; Grimaldi et al., 2019; Käser et al., 2014; Saksena et  
76 al., 2019; Tijerina et al., 2021). However, river bathymetry information, which is essential for  
77 accurate flood modeling, is not available for river networks across large spatial domains. Field  
78 surveys for acquiring bathymetry are impractical for river networks spanning hundreds of  
79 kilometers, while remote sensing techniques such as bathymetric Lidar and photogrammetry are  
80 limited to shallow and clear river reaches only (Feurer et al., 2008; Gao, 2009; Legleiter et al.,  
81 2015; Pan et al., 2015). A useful alternative for large-scale river bathymetry estimation is the  
82 application of conceptual models that can estimate bathymetry based on easily accessible data  
83 using functional surfaces. Several studies have implemented different bathymetric shapes ranging

84 from simplistic symmetric shapes such as rectangles, triangles and parabolas (Czuba et al., 2019;  
85 Grimaldi et al., 2018; Trigg et al., 2009) to more complex functional surfaces based on hydraulic  
86 and geomorphologic concepts (e.g., Bhuyian et al., 2015; Brown et al., 2014; Merwade, 2004;  
87 Price, 2009). These conceptual models try to estimate shapes that reflect certain bathymetric  
88 characteristics of the actual riverbed (such as longitudinal slope, thalweg elevation) while ignoring  
89 other bathymetric characteristics as is the case for channel side-slope (bank slope) when  
90 rectangular channels are implemented. The underlying assumption for implementing these  
91 conceptual bathymetric models as an alternative to detailed bathymetric surveys in H&H models  
92 is that they contain just enough bathymetric detail to produce acceptable H&H simulations. Such  
93 an assumption requires a comprehensive understanding of the effect of bathymetric representation  
94 on flooding related physical processes to ensure that essential bathymetric characteristics are  
95 accurately incorporated.

96         Several studies have analyzed the effect of bathymetry on channel hydrodynamics (Dey et  
97 al., 2019; Grimaldi et al., 2018; Saleh et al., 2012; Trigg et al., 2009), but they have ignored the  
98 effect of bathymetry on subsurface hydrological processes, especially for tightly coupled H&H  
99 models spanning large spatial domains. Prior works exploring the impact of river bathymetry on  
100 surface-subsurface interactions have been conducted on relatively small spatial scales such as  
101 across a meander or along a single reach. For example, Chow et al. (2018) used field measurements  
102 to show that appropriate representation of asymmetry in channel geometry is critical for accurate  
103 estimation of hyporheic exchanges at a river meander. Doble et al., (2012) demonstrated that the  
104 surface-subsurface interactions in the vicinity of the river are affected by the side-slope of river  
105 channels (riverbank slope) for a field-scale study. Similarly, Mejia and Reed (2011) demonstrated  
106 the importance of bathymetry in single reaches by implementing a loosely coupled hydrologic and

107 hydraulic modeling framework. These studies have shown that river bathymetry impacts the  
108 surface-subsurface hydrodynamics at the reach scale. Hydrologic and hydrodynamic processes  
109 aggregate and interact differently as we move from single reach to large river networks spanning  
110 an entire watershed (Saksena et al., 2021). Therefore, there is a need to evaluate the influence of  
111 river bathymetry on hydrologic processes across large river networks. Addressing this need is  
112 critical for enabling effective and parsimonious incorporation of river bathymetry in regional or  
113 continental scale models for flood simulations.

114         Considering the above discussion, the overarching aim of this study is to provide a  
115 comprehensive understanding of the impact of river bathymetry on flooding-related surface and  
116 subsurface processes at a river network scale. Prior studies investigating this topic have either  
117 focused on river bathymetry's effect on channel routing only, thereby ignoring the interdependence  
118 between surface and subsurface processes including SW-GW interactions or explored its effect on  
119 within reach subsurface hydrological processes at small spatial scales (reach scale or smaller). This  
120 study overcomes the limitations of prior studies by creating large-scale physically-based  
121 distributed models to demonstrate that the effect of river bathymetry on not just fluvial channel  
122 routing, but also SW – GW interactions and infiltration. Past studies have shown how the lack or  
123 inclusion of river bathymetry impacts the flood inundation estimation, but this study aims to shed  
124 light on its effect on the physical process affecting flood simulation across a river network thereby  
125 facilitating efficient bathymetry incorporation for accurately simulating large-scale flooding-  
126 related surface and subsurface processes in data-sparse regions. Specifically, the objectives of this  
127 study are to: (i) quantify the effect of river bathymetry incorporation on surface and subsurface  
128 physical processes, including their interactions, across large river networks; and (ii) identify  
129 specific bathymetric characteristics, such as channel conveyance, channel asymmetry and channel

130 thalweg, that control surface and subsurface physical processes in floodplains. These objectives  
131 are accomplished by simulating the hydrology and hydrodynamics of two watersheds and  
132 analyzing the fluxes for four different levels of bathymetric details across the river network.

## 133 **2 Study Area and Data**

134 The objectives presented in Introduction can be accomplished by using watersheds that are  
135 expected to produce significantly different SW-GW interactions. Accordingly, we selected two  
136 study areas in Indiana, presented in Figure 1(a) and Table 1, with distinct geomorphic, soil and  
137 land use characteristics, but similar climatological and geologic characteristics. The first study area  
138 is a portion of the Upper Wabash River Basin (referred to as the UWR) with an area of 1,757 km<sup>2</sup>.  
139 This study area contains the Wabash River, extending from the city of Logansport to Lafayette,  
140 and three major tributaries: Tippecanoe River, Wildcat Creek, and Deer Creek. These four streams  
141 vary in length, average width, and depth (Table 1). Additionally, Tippecanoe River and Wildcat  
142 Creek are highly sinuous compared to Wabash River and Deer Creek. This region has experienced  
143 several extreme events in 2005, 2008, 2013 and 2018, causing widespread flooding. The geology  
144 of the region consists of glacial till deposits, fertile soils, and shallow aquifers, with a deep  
145 confining layer of shale (Saksena and Merwade, 2017b). While there are some developed regions  
146 around Lafayette and Logansport, the area is primarily agricultural with high percentage of forest  
147 and agricultural land use in the floodplains as presented in Table 1.

148 The second study area, with an area of 370 km<sup>2</sup>, is a part of the White River Basin (referred  
149 to as WHR), encompassing the City of Indianapolis and contains three major tributaries: Fall  
150 Creek, Williams Creek, and Crooked Creek. The streams in this area have smaller variability in  
151 geomorphologic characteristics (Table 1) compared to UWR. For example, the White River,  
152 Williams Creek and Crooked Creek all have similar sinuosities. Because this region is highly

153 urbanized, there are several drop structures, artificial lakes, and detention ponds in the floodplain  
154 of the White River. Additionally, the developed regions in the floodplain of White River are  
155 protected by levees.

156 Topography, surface roughness (Manning's  $n$ ), and upstream boundary conditions are the  
157 primary inputs to hydrodynamic models, and so we obtained high-quality Lidar-based DEMs for  
158 both study areas from the Indiana Spatial Data Portal (ISDP). Additionally, bathymetric survey  
159 data are available for 26 cross-sections near the Tippecanoe-Wabash confluence (Figure 2). The  
160 DEM resolution for UWR and WHR is 9 m and 3 m, respectively. A relatively coarser DEM is  
161 used for UWR to address the computational constraints due to its size, which is approximately 5  
162 times larger compared to WHR. The analysis presented here primarily focuses on comparison of  
163 differences in hydrologic and hydrodynamic fluxes due to differences in bathymetric  
164 configurations in the same watershed. The DEM resolution used for creating different models  
165 belonging to a specific watershed remains unchanged to ensure consistency in comparing results  
166 from models with different bathymetric configurations. Additionally, the DEM resolutions for both  
167 watersheds are within the hyper-resolution range ( $< 10\text{m}$ ) for flood models and are not expected  
168 to affect the results.

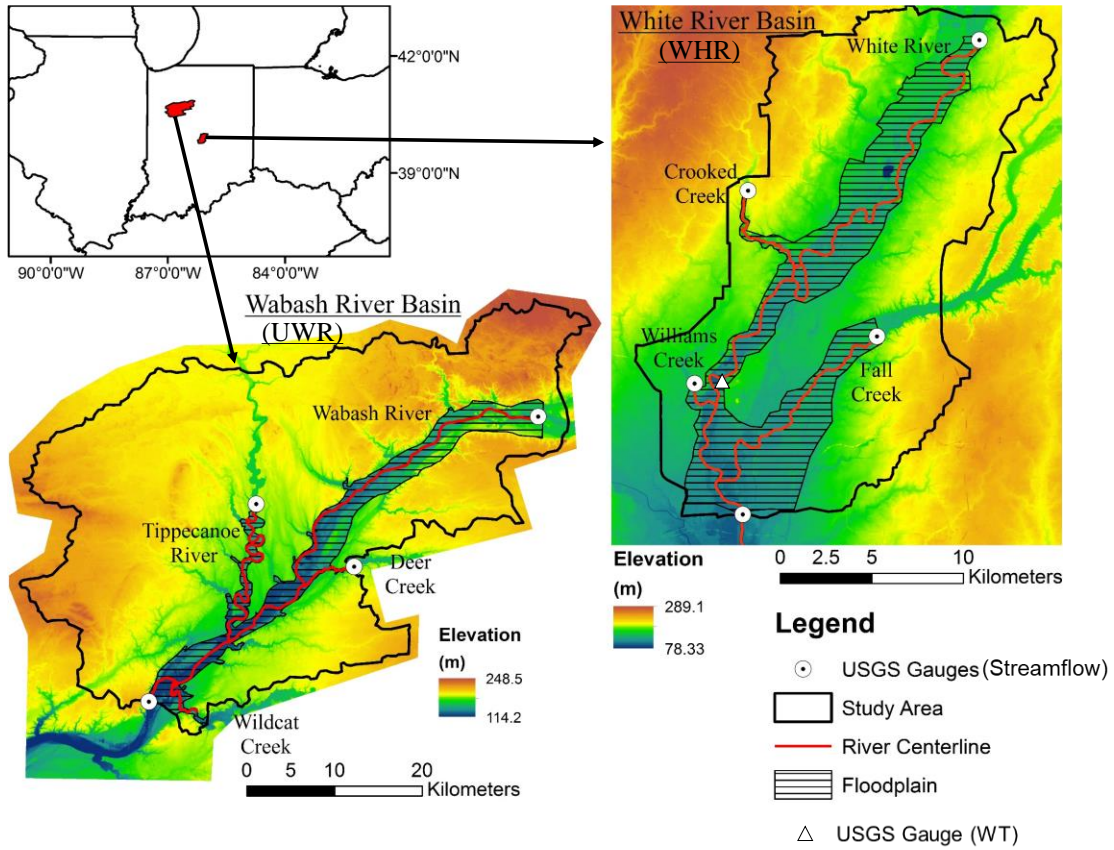
169

170

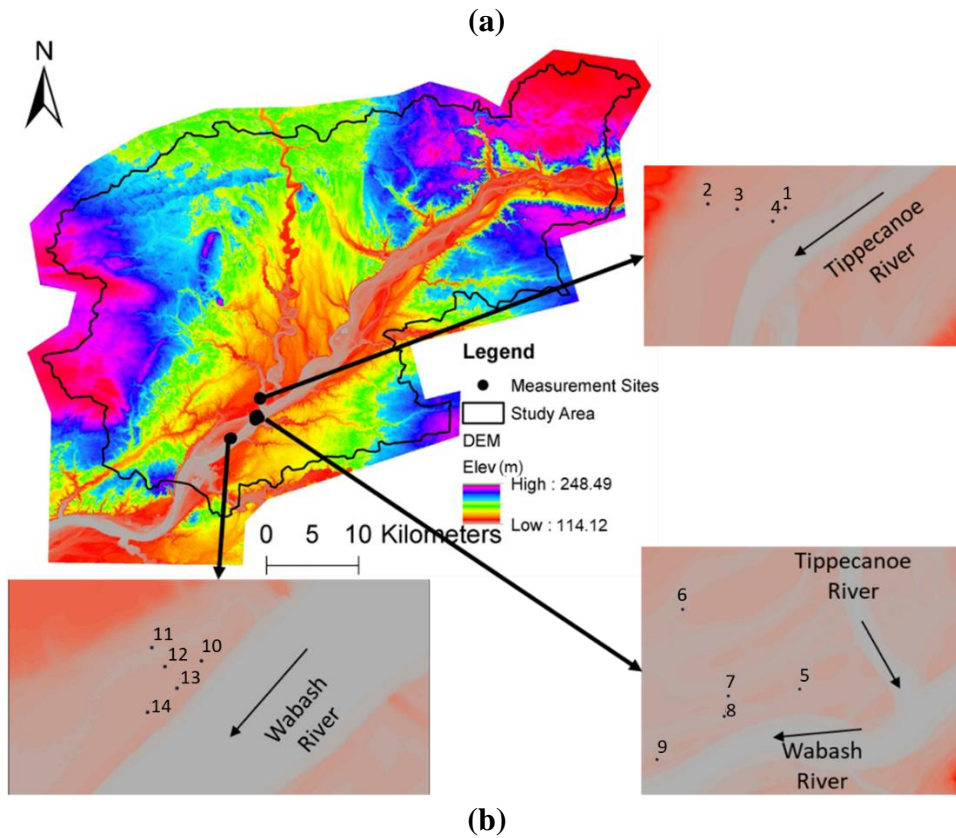
**Table 1.** Study area description

<b>Geomorphological Characteristics</b>					
<u>UWR</u>					
<i>Name</i>	<i>Length (km)</i>	<i>Average Width (m)</i>	<i>Average Depth (m)</i>	<i>Slope (<math>\times 10^{-3}</math>)</i>	<i>Sinuosity</i>
Wabash River	83.01	136.0	1.74	0.3	1.22
Tippecanoe River	30.76	84.2	1.52	0.5	1.93
Wildcat Creek	8.59	54.6	0.70	0.7	2.06
Deer Creek	8.03	34.6	0.76	1.2	1.28
<u>WHR</u>					
<i>Name</i>	<i>Length (km)</i>	<i>Average Width (m)</i>	<i>Average Depth (m)</i>	<i>Slope (<math>\times 10^{-3}</math>)</i>	<i>Sinuosity</i>
White River	42.8	83.2	1.58	0.4	1.48
Fall Creek	14.8	40.9	0.86	1.0	1.26
Williams Creek	7.3	13.3	1.43	3.1	1.48
Crooked Creek	2.5	15.6	1.45	2.3	1.49
<b>Landuse as per NLCD 2011 (%)</b>					
<i>Type</i>	<i>UWR</i>		<i>WHR</i>		
	<i>Study Area</i>	<i>Floodplain</i>	<i>Study Area</i>	<i>Floodplain</i>	
Agricultural	77	50	3	4	
Forest	12	27	4	7	
Water	2	9	3	9	
Urban/Developed	10	14	89	81	
<b>Soil Group as per NRCS gSSURGO (%)</b>					
<i>Soil Type</i>	<i>UWR</i>		<i>WHR</i>		
A	13.8		0.1		
B	56.2		51.5		
C	29.8		48.3		
D	0.2		0.1		

171



172  
173

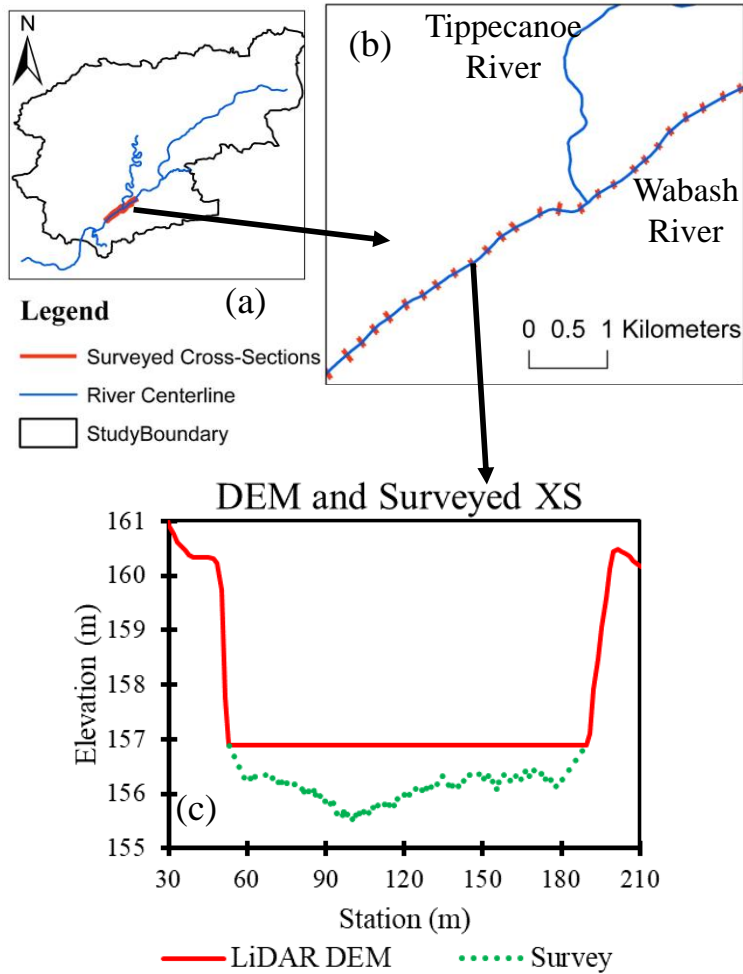


174  
175  
176

**Figure 1.** (a) Location map of the study areas and (b) field survey sites for GWT at UWR

177           The distributed hydrologic modeling approach used in this study requires data related to  
178 land use, streamflow, rainfall, soil properties and aquifer characteristics. The land use data are  
179 obtained from the National Land Cover Database (NLCD) from the Natural Resources  
180 Conservation Service (NRCS). The roughness values (Manning's  $n$ ) for the different land use  
181 classes in the study areas are obtained from Saksena and Merwade (2015). The upstream boundary  
182 condition for each stream is determined by incorporating streamflow hydrographs obtained from  
183 United States Geologic Survey (USGS) gages, which also provide river depth information at those  
184 locations. The rainfall data are obtained from the North American Land Data Assimilation System  
185 (NLDAS) at a 12-km grid resolution. The soil types are characterized using the Hydrologic Soil  
186 Group (HSG) classification provided in NRCS's Gridded Soil Survey Geographic database  
187 (gSSURGO).

188           The outlet of UWR (shown in Figure 1(a)) is located at the USGS gage 03335500 Wabash  
189 River at Lafayette, IN, and the outlet for the WHR is located at the USGS gage 03353000, White  
190 River at Indianapolis, IN. These outlet gages are used for validating the physically-based  
191 distributed models used in this study. Additionally, the GW component of the models is validated  
192 using within-reach observations of water table at specific locations. In WHR, there is a USGS  
193 gauge (USGS 394952086110901) which monitors GWT elevation near the White River (Figure  
194 1(a)). However, there is no such continuous GWT monitoring station in UWR. Therefore, site  
195 visits were organized for measuring water table depths at multiple locations in the Wabash River  
196 floodplain and near the Wabash River – Tippecanoe River confluence (Figure 1(b)). The water  
197 table was measured by using 2m deep piezometers in two different seasons: Winter 2018 (16th  
198 Dec 2018) across 8 locations (Points 1, 4, 5, 8 – 10, 13, and 14) and Summer 2019 (24th July 2019)  
199 across 9 locations (Points 2 – 4, 6 – 8 and 11 – 13).



200

201 **Figure 2:** Figure showing (a) the location of surveyed cross-sections in UWR, (b) close-up of the  
 202 surveyed cross-sections, and (c) comparison of one of the surveyed cross-section and LiDAR  
 203 DEM derived cross-section at that location

204

### 205 3 Experimental Design

206 A major constraint in quantifying the impact of river bathymetry impact on watershed  
 207 processes is the absence of bathymetric data for river networks across large spatial domains. In  
 208 this study, first a conceptual bathymetric model (described in Section 4) calibrated with surveyed  
 209 bathymetric data is implemented to create a bathymetric representation comprising of asymmetric  
 210 cross-sections with realistic side slopes (bank slopes). This configuration, with the best 3D river  
 211 network among all configurations, is designated as Control.

212           Next, two more bathymetric configurations are created by reducing the level of detail  
213 incorporated in the 3D river network. One configuration (M1) has a rectangular cross-section that  
214 preserves both the area (channel storage) and the depth (thalweg elevation) of cross-sections as  
215 compared to Control but ignores the side slope and the asymmetry in river cross-sections. It should  
216 be noted that information about channel conveyance capacity (bankfull area) is not readily  
217 available for river networks. However, some studies have developed alternative methods to  
218 estimate the channel conveyance capacity, including drainage area-based regionalization equations  
219 as well as the algorithms developed for the upcoming Surface Water and Ocean Topography  
220 (SWOT) mission (Rodríguez et al., 2020; Schaperow et al., 2019; Yoon et al., 2012). This  
221 configuration can provide insights into the suitability of such parsimonious methods for  
222 incorporating bathymetry as well as the role of channel asymmetry and side slope on subsurface  
223 hydrological processes in large-scale river networks.

224           The next configuration (M2) also has a rectangular cross-section but only preserves the  
225 depth (thalweg elevation) of cross-sections but not the area (channel storage). This configuration  
226 has previously been deployed in studies where sufficient bathymetry data is not available from  
227 boat surveys that only capture the longitudinal channel profile (example: Czuba et al., (2019);  
228 Grimaldi et al., (2018)). Finally, the Lidar derived DEM without any bathymetry incorporation  
229 (M3) is also created. The inclusion of M3 can show what processes are significantly impacted (or  
230 not impacted) by the incorporation of river bathymetry and highlight a potential error source for  
231 H&H models in data sparse regions. This configuration is expected to perform poorly as compared  
232 to the other three configurations. This configuration is included for contextualizing the results of  
233 M1 and M2 with respect to “Control”.

234           These four configurations (Control, M1, M2 and M3) are simulated using a tightly coupled  
235 physically-based distributed model (described in Section 5) capable of capturing the complex  
236 interplay of various hydrologic and hydrodynamic processes that govern the movement of water  
237 in a watershed. The hydrologic and hydrodynamic outputs of M1, M2 and M3 are compared to  
238 those estimated by “Control” to provide insights into the role of bathymetric representation on  
239 surface and subsurface processes in the floodplains of a river network.

240

#### 241 **4 Bathymetric Model Development**

242           Previous studies have implemented a wide range of functional surfaces as approximations  
243 for channel geometry ranging from standard geometrical shapes, such as parabola, rectangle or  
244 exponential curve (Czuba et al., 2019; Grimaldi et al., 2018; Trigg et al., 2009) to more intricate  
245 channel representations based on geomorphological concepts (e.g., Bhuyian et al., 2015; Brown et  
246 al., 2014; Merwade, 2004; Price, 2009). These conceptual models are designed for estimating  
247 bathymetry for a single reach only, which is usually the main stem of a river network. This study  
248 implements a network-scale river bathymetry generation called the System for Producing RIver  
249 Network Geometry (SPRING). Some features of this model have been adapted from Merwade  
250 (2004).

251           SPRING first creates bathymetry for each individual reach (Step-1) following the  
252 procedure of Merwade (2004), and then these reach-scaled bathymetry datasets are joined by  
253 creating bathymetry at river confluences (Phase-2). The end result from SPRING is a 3D  
254 representation of the entire river network which can be burned into the DEM. The bathymetry  
255 generation process for each reach and confluence is briefly described below.

256 *4.1 Bathymetry generation for individual reaches*

257 To estimate the bathymetry of individual reaches, this study adapted the meandering  
 258 thalweg based approach of the River Channel Morphology Model (RCMM: Merwade, 2004)  
 259 because of its ability to account for channel anisotropy. The meandering of the thalweg is primarily  
 260 caused by sediment deposition on the inner bank and erosion at the outer bank of a river bend. This  
 261 process is conceptualized to create a set of equations (Equations 1-3) that can approximate a  
 262 channel cross-section (Figure 3). The inputs, in this case, are channel centerline, banks, DEM, and  
 263 depth of the river at multiple locations along the channel network. The methodology, adopted from  
 264 Merwade (2004) and Dey et al., (2019), is described briefly in *Appendix A1*.

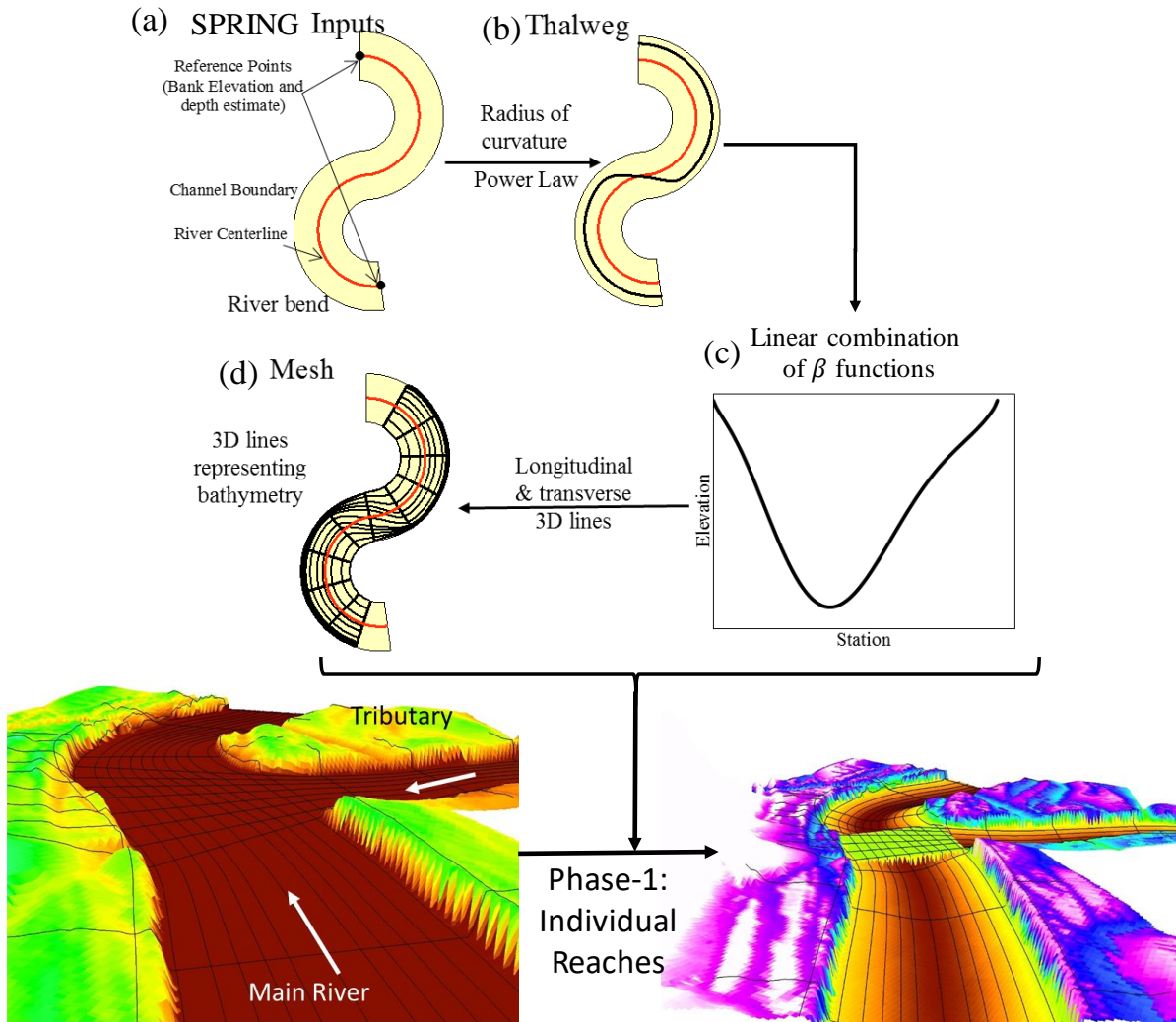
$$265 \quad t^* = \begin{cases} a(r^*)^{-b} - 0.5, & r^* \leq 2 \\ 0, & r^* > 2 \end{cases} \quad (\text{Equation 1})$$

$$266 \quad z^*(n^*) = \{f(n^*|\alpha_1, \beta_1) + f(n^*|\alpha_2, \beta_2)\} \times k \quad (\text{Equation 2})$$

$$267 \quad z(n^* \times W) = z_{bank} - z^*(n^*) \times depth \quad (\text{Equation 3})$$

268 where,  $r^*$  is the normalized radius of curvature of a river segment ( $r^* = r/w$ ),  $t^*$  is the  
 269 normalized thalweg location at a cross-section ( $t^* = t/w$ ),  $w$  is the average width of the river  
 270 segment,  $a$  and  $b$  are constants,  $z^*$  is the normalized depth of the channel bed at a distance  $n^*$   
 271 along the cross-section from the center of the channel,  $f(n^*|\alpha_1, \beta_1)$  is the beta probability  
 272 distribution function (pdf) with parameters  $\alpha_1$  and  $\beta_1$ ,  $f(n^*|\alpha_2, \beta_2)$  is the beta pdf with parameters  
 273  $\alpha_2$  and  $\beta_2$  and  $k$  is a scaling parameter. Using a linear combination of two beta pdfs enables  
 274 SPRING to model asymmetric cross-section shapes by varying its parameters. The parameters of  
 275 SPRING ( $a, b, \alpha_1, \alpha_2, \beta_1, \beta_2$ ) are calibrated using surveyed cross-sections using the Particle Swarm  
 276 Optimization technique.

277



278

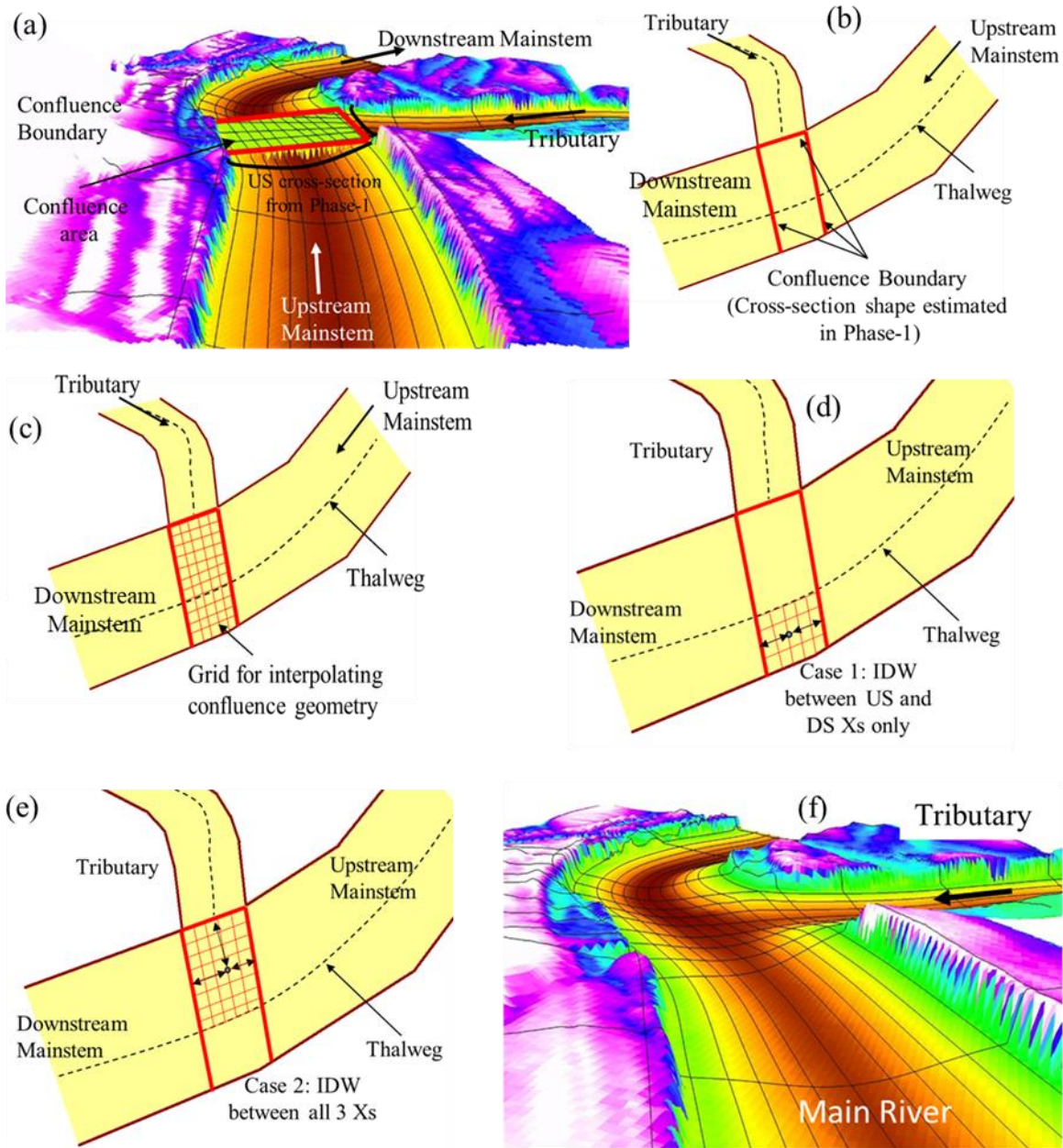
279 **Figure 3.** Workflow of SPRING to estimate bathymetry at individual reaches. (a) The input  
 280 datasets; (b) estimating meandering thalweg from the radius of curvature of river centerline using  
 281 Equation (1); (c) Estimating asymmetric cross-sections using Equations (2) and (3); and (d)  
 282 creating a mesh to generate 3D representation of individual reaches. Note: Part of the figure is  
 283 adapted from Dey, (2016).  
 284

285 In the curvilinear axes adopted in this study, the lateral axis (running from left to right bank  
 286 perpendicular to the centerline) is positive on the right side and negative on the left side when  
 287 looking down the direction of flow of the river Merwade (2004). The center and radius of curvature  
 288 ( $r$ ) are determined by the three-point arc method. If the center of curvature lies to the left of the  
 289 centerline, it means the river at the meander is turning to the left and the thalweg is located to the

290 right side of the centerline (positive  $t^*$ ) and vice-versa. The elevation of the thalweg along the  
291 channel is estimated by linearly interpolating the thalweg elevation between “reference points”  
292 which are specified at locations where such information is available. Therefore, SPRING creates  
293 a piecewise linear thalweg profile with the reference points acting as points where the thalweg  
294 slope changes. Usually, reference points should be provided at the upstream and downstream ends  
295 of each reach, but SPRING can accommodate multiple references points along the same reach as  
296 well.

#### 297 *4.2 Bathymetry generation at confluence*

298       Once the bathymetry for individual reaches has been estimated, the next step is to connect  
299 these individual reaches by estimating the bathymetry at the river confluences. Figure 4 depicts  
300 the methodology for estimating the confluence boundary. First, SPRING locates the confluence as  
301 the point of intersection of three or more reach centerlines. It, then, categorizes the three centerlines  
302 as “downstream mainstem”, “upstream mainstem” and “tributary” channels (Figure 4(a)). This is  
303 decided based on the start and end point of the three centerlines and the drainage areas of each of  
304 the reaches draining into the confluence. The stream with the lowest drainage area is designated  
305 as a tributary. The reach downstream of the confluence is designated as the downstream mainstem.  
306 Next SPRING joins the banks of each stream to create the “confluence boundary” (Figure 4(b)).  
307 The region enclosed by the confluence boundary is used for estimating bathymetry at the  
308 confluence.



309

310 **Figure 4.** Figure showing the workflow for estimating channel geometry at confluences. (a) The  
 311 input for Phase-2 (output of Phase-1); (b) estimating confluence boundary; (c) creating grid  
 312 across confluence area; (d) interpolating geometry for Case-1 (Equation 4) for points on the other  
 313 side of thalweg as the tributary; (e) interpolating geometry for Case-2 (Equation 4) for points on  
 314 the same side of thalweg as the tributary, and (f) final output with hydraulically connected  
 315 confluence geometry.

316

317

318

To estimate the bathymetry at the confluence, a variation of the inverse distance weighting

(IDW) algorithm is used. SPRING creates a mesh of equidistant longitudinal lines running parallel

319 and transverse to the mainstem thalweg inside the confluence boundary (Figure 4(c)). For each  
 320 point on the mesh, SPRING locates the closest point on each boundary cross-section. The  
 321 elevations of these points on the boundary cross-sections are known from the reach bathymetry  
 322 estimated in the first step (Section 3.1). The boundary cross-sections are expected to differ in  
 323 geometry and maximum depth, due to the differences in drainage areas upstream and downstream  
 324 of the confluence for the mainstem as well as variations in river characteristics between the  
 325 tributary and the mainstem. SPRING is designed to account for these variations in the geometry  
 326 of boundary cross-sections while interpolating the bathymetry at confluences.

327 If the mesh point is on the other side of the mainstem thalweg as compared to the tributary  
 328 (Figure 4(d)), a two-point IDW is implemented between the upstream and downstream boundary  
 329 cross-sections of the main stem (Case 1 in Equation 4). For mesh points lying on the same side of  
 330 the mainstem thalweg as the tributary (Figure 4(e)), a three-point IDW is implemented to estimate  
 331 the elevation of the mesh point as shown in Equation 4 (Case 2).

$$332 \quad z = \begin{cases} \frac{z_1 d_1^{-1} + z_2 d_2^{-1}}{d_1^{-1} + d_2^{-1}}, & \text{Case 1} \\ \frac{z_1 d_1^{-1} + z_2 d_2^{-1} + z_3 d_3^{-1}}{d_1^{-1} + d_2^{-1} + d_3^{-1}}, & \text{Case 2} \end{cases} \quad (\text{Equation 4})$$

333 where  $z$  is the elevation of the current point in confluence mesh for which elevation is being  
 334 estimated,  $z_1$ ,  $z_2$  and  $z_3$  are the elevations of the points closest to the current point on the cross-  
 335 sections upstream of confluence in the main river, downstream of the confluence in the main river  
 336 and in the tributary just upstream of the confluence respectively, and  $d_1$ ,  $d_2$  and  $d_3$  are the distances  
 337 of these three points from the current point. This process is repeated for all points in the confluence  
 338 mesh to create a 3D representation of the confluence bathymetry.

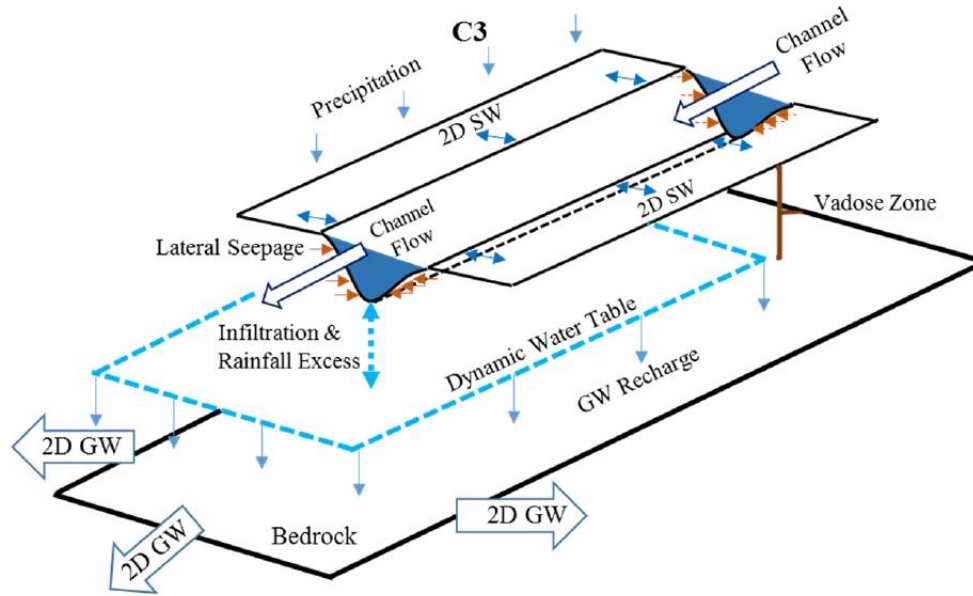
339 The 3D mesh of the individual reaches and confluences together create a synthetic  
 340 representation of bathymetry for the entire river network. The 3D mesh is converted to a DEM

341 using the Natural Neighbor interpolation technique. The final step involves burning this 3D mesh-  
342 derived raster into the raw DEM (Lidar) to generate a DEM with improved bathymetric  
343 representation.

## 344 **5 Physically-based Distributed Model Description**

345 In this study, physically-based Interconnected Channel and Pond Routing (ICPR) model  
346 (Saksena et al., 2020, 2019) that incorporates flood-related processes such as rainfall-runoff,  
347 infiltration, and SW-GW interactions in addition to surface routing is used (Figure 5). ICPR uses  
348 a flexible mesh structure to represent both the surface and the subsurface. The surface mesh  
349 comprises of 1D elements in the river channel and 2D elements elsewhere, and the subsurface is  
350 divided into three layers with each layer represented by a 2D mesh. The soil parameters governing  
351 the subsurface are tabulated in Table 2. At each timestep, the hydrology and hydraulics are  
352 simulated across each element of the surface mesh. Simultaneously, it computes the subsurface  
353 processes across the subsurface mesh and the interactions between the surface and subsurface  
354 meshes. Therefore, it can capture the interplay among surface hydrology, river hydrodynamics and  
355 subsurface processes, making it ideal for this study. For more information on ICPR and its  
356 implementation, please refer to the Appendix A-2 or the “C3” configuration in Saksena et al.,  
357 (2019) or Saksena et al., (2020).

358



359

360 **Figure 5.** Conceptual illustration of physically based distributed modeling in ICPR (adapted  
 361 from Saksena et al., (2019))

362 **Table 2:** Table of initial soil parameters in ICPR (adapted from Saksena et al., (2019)).  $K_v$  is  
 363 vertical hydraulic conductivity, MC is the moisture content (fraction), PSI is the pore size index  
 364 (dimensionless), and  $\Psi$  is the soil matric potential.

Vadose Zone	Soil Type	$K_v$ (mm/hr)	Saturated MC	Residual MC	Initial MC	Field Capacity MC	Wilting Point MC	PSI	$\Psi$ (cm)
Layer 1 50 cm	A	15.24	0.300	0.069	0.128	0.128	0.107	0.518	38.3
	B	6.20	0.540	0.061	0.200	0.200	0.138	0.620	25.5
	C	2.34	0.458	0.051	0.300	0.300	0.225	0.296	59.2
	D	1.40	0.620	0.053	0.240	0.240	0.118	0.161	197.9
Layer 2 50 cm	A	8.38	0.277	0.040	0.125	0.125	0.063	0.296	59.2
	B	3.10	0.280	0.070	0.170	0.170	0.135	0.316	67.5
	C	1.17	0.320	0.078	0.220	0.220	0.155	0.270	106.8
	D	0.80	0.360	0.080	0.200	0.200	0.090	0.161	197.9
Layer 3 50 cm	A	2.10	0.120	0.030	0.090	0.090	0.060	0.540	30.7
	B	0.77	0.200	0.040	0.100	0.100	0.040	0.226	99.8
	C	0.29	0.180	0.045	0.120	0.120	0.075	0.161	168.4
	D	0.20	0.190	0.045	0.090	0.090	0.060	0.161	197.9
GW Zone	Type	Effective Porosity, $\eta_e$		Hydraulic Conductivity, K (mm/hr)					
Aquifer	A	0.175		30.48					
	B	0.270		12.40					
	C	0.310		4.67					
	D	0.360		6.35					

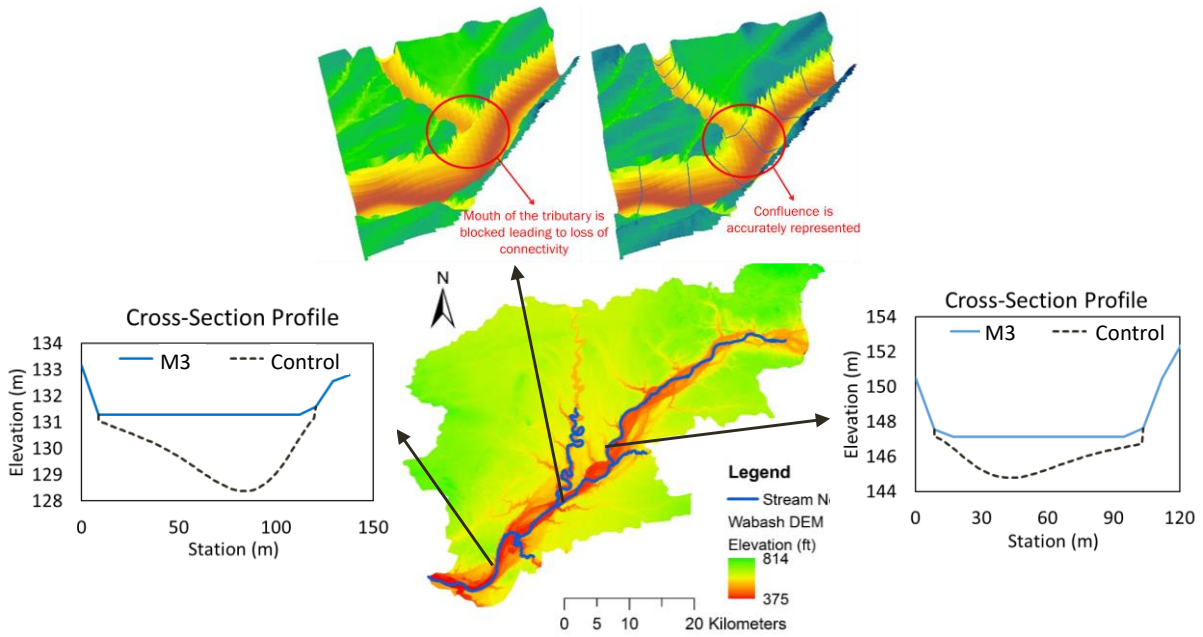
365

366 UWR is simulated for two continuous simulations events from 18th February 2016 to 30th  
367 April 2016 (72 days) and 10th February 2018 to 15th May 2018 (94 days). WHR is simulated for  
368 a one-month period from 25th May 2015 to 25th June 2015. The first 120 hours (5 days) for each  
369 simulation are used as model warmup period. The model parameters have not been calibrated and  
370 have been kept consistent across all four bathymetric configurations. Earlier studies using ICPR  
371 (Saksena et al., 2019; Saksena and Merwade, 2017a) have shown that the model is capable of  
372 producing accurate results without parameter calibration when the watershed's physical  
373 description is adequately captured in the model with high-resolution input of surface and sub-  
374 surface characteristics. Additionally, model calibration would alter the parameters to account for  
375 any shortcomings in the simulation of hydrologic or hydraulic processes for the different  
376 bathymetric configurations, thus affecting the model's behavior and rendering comparison of  
377 model outputs inconsistent.

## 378 **6 Results and Discussion**

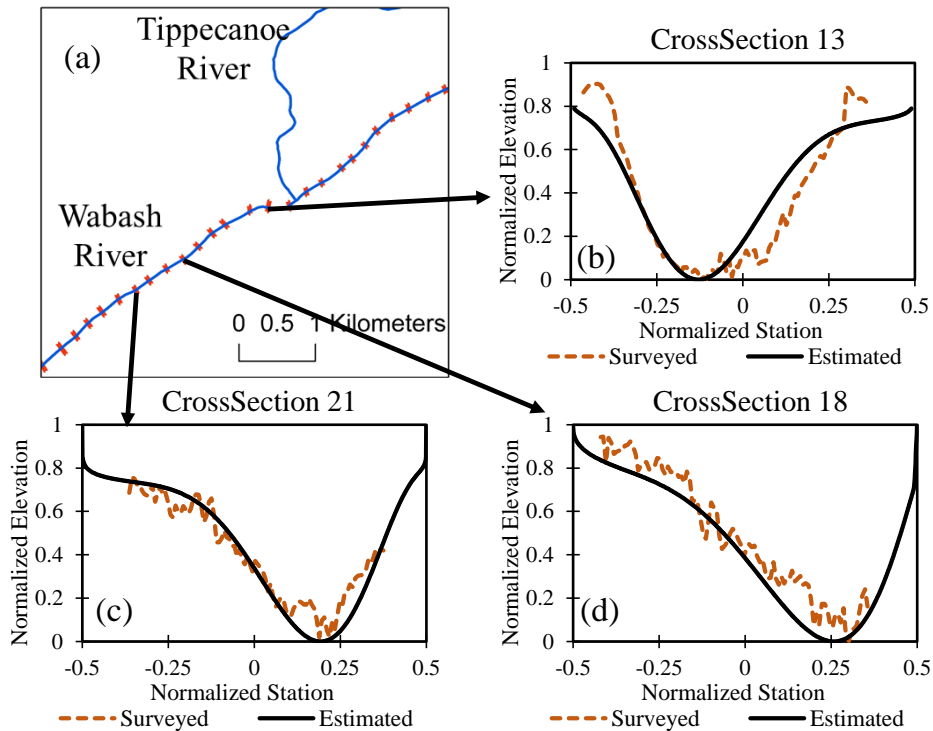
### 379 *6.1 Bathymetry Incorporation*

380 SPRING, described in Section 4, is implemented at both UWR and WHR to create DEMs  
381 with a complete 3D representation of river network bathymetry. The channel centerline and banks  
382 are digitized manually using the DEM and aerial imagery. The USGS gages provide depth of  
383 channel bed at gaged locations, which are then interpolated to create channel depth at unknown  
384 points along a river. The parameters of SPRING are calibrated using surveyed cross-sections.  
385 Figure 6 shows the change in cross-sections and confluence bathymetry for the two basins as  
386 estimated by SPRING while Figure 7 shows a comparison of the SPRING generated cross-sections  
387 for Control with surveyed cross-sections.



388  
 389 **Figure 6** Examples of SPRING generated cross-sections exhibiting asymmetry in “Control”  
 390 configuration and confluence topography incorporated in UWR

391



392  
 393  
 394 **Figure 7** Comparison of surveyed and SPRING estimated cross-section shapes for “Control” at  
 395 different locations along the Wabash River.  
 396

397 Table 3 shows the comparison of the channel characteristics, namely channel conveyance  
 398 capacity (volume) and surface area of the three bathymetric configurations (M1, M2 and M3) with  
 399 Control. Control and M1 have the same channel conveyance capacity but have different shapes,  
 400 which leads to a difference of 0.7% in surface areas of these two networks. M1 and M2 have the  
 401 same surface area but M2's channel conveyance capacity is 34.7% and 27.5% higher than Control  
 402 (and M1) for UWR and WHR, respectively. The significantly larger differences in channel  
 403 conveyance capacity as compared to the surface area among the bathymetric configurations is an  
 404 effect of the high channel width to channel depth ratio for natural channels. Since natural river  
 405 channels are much wider than they are deeper, the cross-sectional perimeter tends to be similar to  
 406 the top width of the channel. Finally, M3 has the lowest surface area and channel conveyance  
 407 capacity due to incomplete channel representation in the Lidar-derived DEMs.

408 **Table 3.** Percentage change in bathymetric characteristics of M1, M2 and M3 with respect to  
 409 Control for the two study areas.

Study Area	Bathymetric Characteristic	Bathymetric Configuration		
		M1	M2	M3
UWR	Volume	0.0	34.7	-18.0
	Surface Area	3.1	3.1	-0.7
WHR	Volume	0.0	27.5	-27.5
	Surface Area	6.4	6.4	-0.7

410  
 411 Table 4 shows the change in longitudinal channel slope because of the incorporation of  
 412 bathymetry. Except for Wildcat Creek in UWR, the change in slope is less than 4% for all other  
 413 streams. SPRING generated channel networks have a piece-wise linear longitudinal profile with  
 414 the upstream and downstream ends of the reaches having different depths due to differences in  
 415 drainage areas at the two ends. Therefore, Control, M1 and M2 have identical slopes for each reach  
 416 which is higher than the slopes of the reaches in M3.

417 **Table 4.** Change in longitudinal slope for each river due to bathymetry incorporation (Control,  
 418 M1 and M2)

<b>River Name</b>	<b>Slope in Control, M1 and M2 (<math>\times 10^{-4}</math>)</b>	<b>Slope in M3 (<math>\times 10^{-4}</math>)</b>	<b>% Change</b>
<u><i>UWR</i></u>			
Wabash River	3.24	3.23	0.4
Tippecanoe River	5.02	4.90	2.4
Deer Creek	12.33	11.94	3.3
Wildcat Creek	7.09	6.39	10.9
<u><i>WHR</i></u>			
White River	4.13	4.08	1.3
Fall Creek	9.57	9.49	0.9
Williams Creek	30.85	30.82	0.1
Crooked Creek	22.57	22.32	1.1

419

## 420 *6.2 Validating Control*

421 The model structure and parameters adopted in this study are validated by comparing the  
 422 outlet streamflow and water table elevations estimated by Control against observed data. Figure 8  
 423 shows the comparison of outlet hydrographs of Control for the three events and the observed  
 424 hydrographs from USGS gauges at those locations. The performance of Control is also quantified  
 425 using four performance metrics – the Nash-Sutcliffe Efficiency (NSE) (Nash and Sutcliffe, 1970),  
 426 Percent Bias (PBias), ratio of the root mean square error to the standard deviation of measured  
 427 data (RSR) and error in magnitude of highest peak flow, which are tabulated in Table 5. RSR is a  
 428 ratio of error in model estimate to variation in observed time-series which helps in comparing  
 429 RMSE across different bathymetric configurations and hydrologic outputs (timeseries). Control

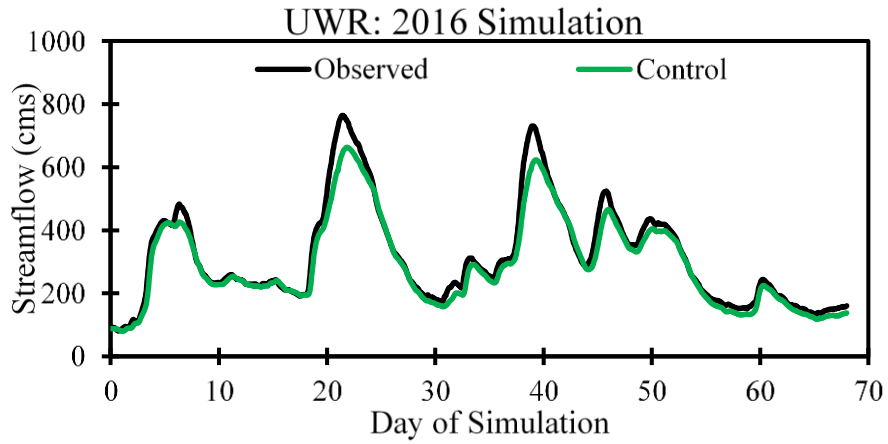
430 exhibits high NSE and low PBias, RSR and error in peak streamflow which indicates the  
 431 acceptable performance of Control for all three events across the two basins.

432 **Table 5:** Performance statistics for validating Control using USGS gauge measured streamflow  
 433 at outlets and GWT timeseries

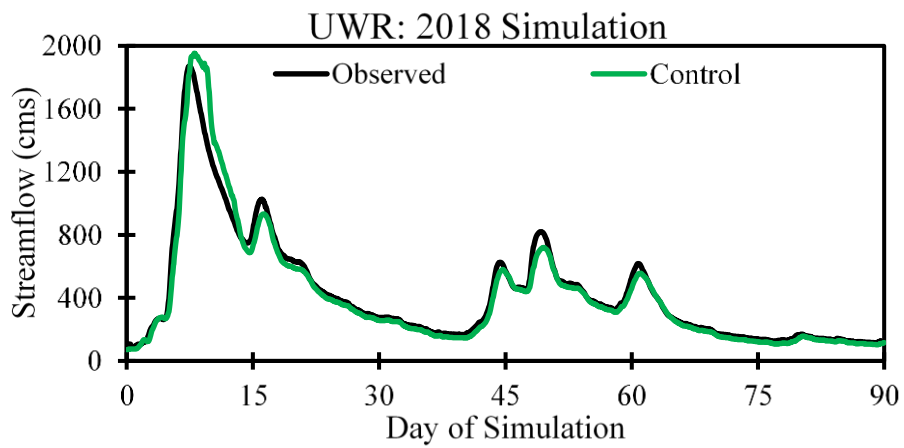
Simulation	Timeseries	NSE	PBias (%)	RSR	Error in Peak (%) *
UWR (2016)	Outlet Hydrograph	0.95	-7.2	0.23	-13.3
UWR (2018)	Outlet Hydrograph	0.96	-2.9	0.21	4.3
WHR (2015)	Outlet Hydrograph	0.95	-4.9	0.23	-8.7
WHR (2015)	GWT Elevation	0.77	-0.08	0.48	0.05

434 \*Error in peak corresponds to the highest peak in the simulation period

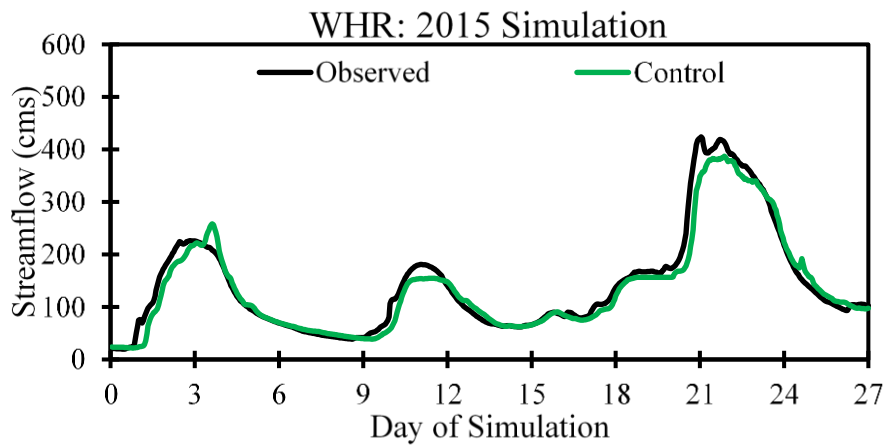
435 The GW component of Control is validated by comparing GWT elevation estimates against  
 436 GWT measurements (Figure 9). For WHR, GWT elevation timeseries observed at a USGS well is  
 437 compared with the GWT estimates at that location for the 2015 simulation (Figure 9(c)) and the  
 438 performance statistics are tabulated in Table 5. In the absence of USGS gauges measuring GWT  
 439 in UWR, GWT is measured at 17 select locations in the floodplains of UWR by using 2m deep  
 440 piezometers. Control was simulated for 21 days including the day of measurements and the GWT  
 441 estimates were compared against those obtained from the piezometers. Out of these 17 datapoints,  
 442 one measurement was reported as flooded (water table at the surface), and the water table was  
 443 found to be deeper than 2 m (depth of piezometers) for seven cases. In all these eight cases, Control  
 444 results corresponded with the observed situations. Comparison of the observed and estimated  
 445 GWT elevations for the remaining nine observations where the GWT depth was within 2m is  
 446 shown in Figure 9(b). RMSE for the simulated water table elevations is 0.43 m.



(a)



(b)



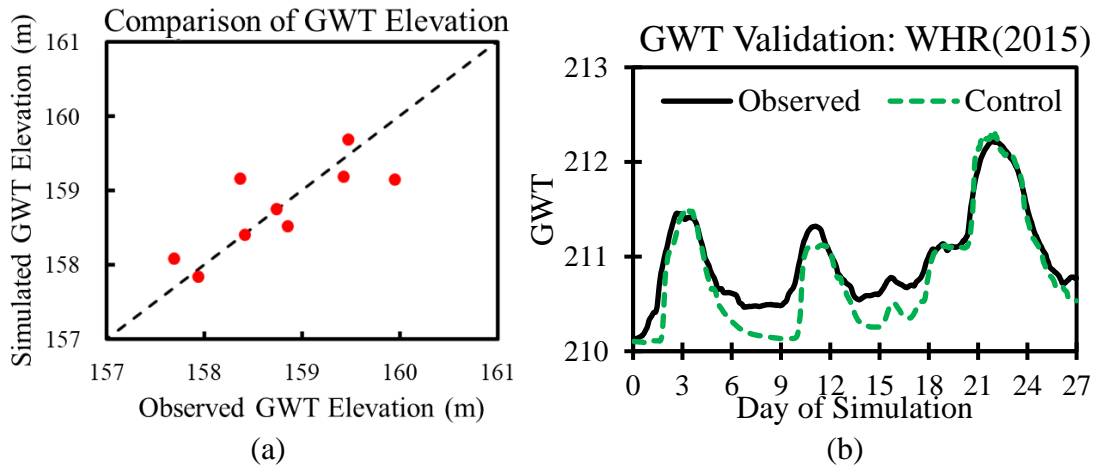
(c)

**Figure 8:** Comparison of outlet hydrograph of Control with observed hydrographs at the outlet of UWR for (a) 2016 simulation, (b) 2018 simulation, and (c) WHR for 2015 simulation.

447  
448  
449  
450  
451

452 The aim of the validation is not to demonstrate that the model structure and parameters are  
 453 accurate; rather the validation demonstrates that the model structure and parameters reasonably  
 454 characterize the surface and subsurface hydrological processes. The overall performance with  
 455 respect to the water table and outlet hydrograph suggests that Control can realistically approximate  
 456 the surface and subsurface hydrological processes. Additionally, the SW-GW model structure  
 457 (mesh resolution) adopted in this study follows the guidelines proposed in Saksena et al (2021) for  
 458 effectively capturing SW-GW interactions in tightly coupled models by considering the intrinsic  
 459 scales of the surface and subsurface processes in the model structure. It should be noted that the  
 460 surface and sub-surface parameters are uncalibrated and are identical across different bathymetric  
 461 configurations to avoid biasing the parameters towards any particular configuration. Therefore,  
 462 changing the bathymetric representation while keeping the model structure and parameters  
 463 constant enables consistent comparison across different bathymetric configurations and provide  
 464 insights into the role of bathymetry in simulating SW-GW interactions.

465



466

467

468 **Figure 9.** Figure showing (a) the comparison of observed and simulated GWT for 9 locations in  
 469 UWR where GWT depth is less than 2m, and (b) the comparison of observed and simulated  
 470 GWT elevation timeseries for WHR at a USGS well.

471

472

473 *6.3 Effect on Overland Flow*

474 To analyze the effect of bathymetry on surface routing, the streamflow hydrographs  
 475 estimated at the outlets and the maximum inundation area estimated by M1, M2 and M3 are  
 476 compared with those estimated by Control. While streamflow at the outlet is not entirely  
 477 representative of the watershed response, especially for medium to large watersheds, it is a useful  
 478 indicator of the overall water balance across different simulations. Figure 10 shows the streamflow  
 479 hydrographs at the outlet for all three events corresponding to all four configurations. The relevant  
 480 performance metrics for quantifying the performance of M1, M2 and M3 with respect to Control  
 481 are tabulated in Table 6.

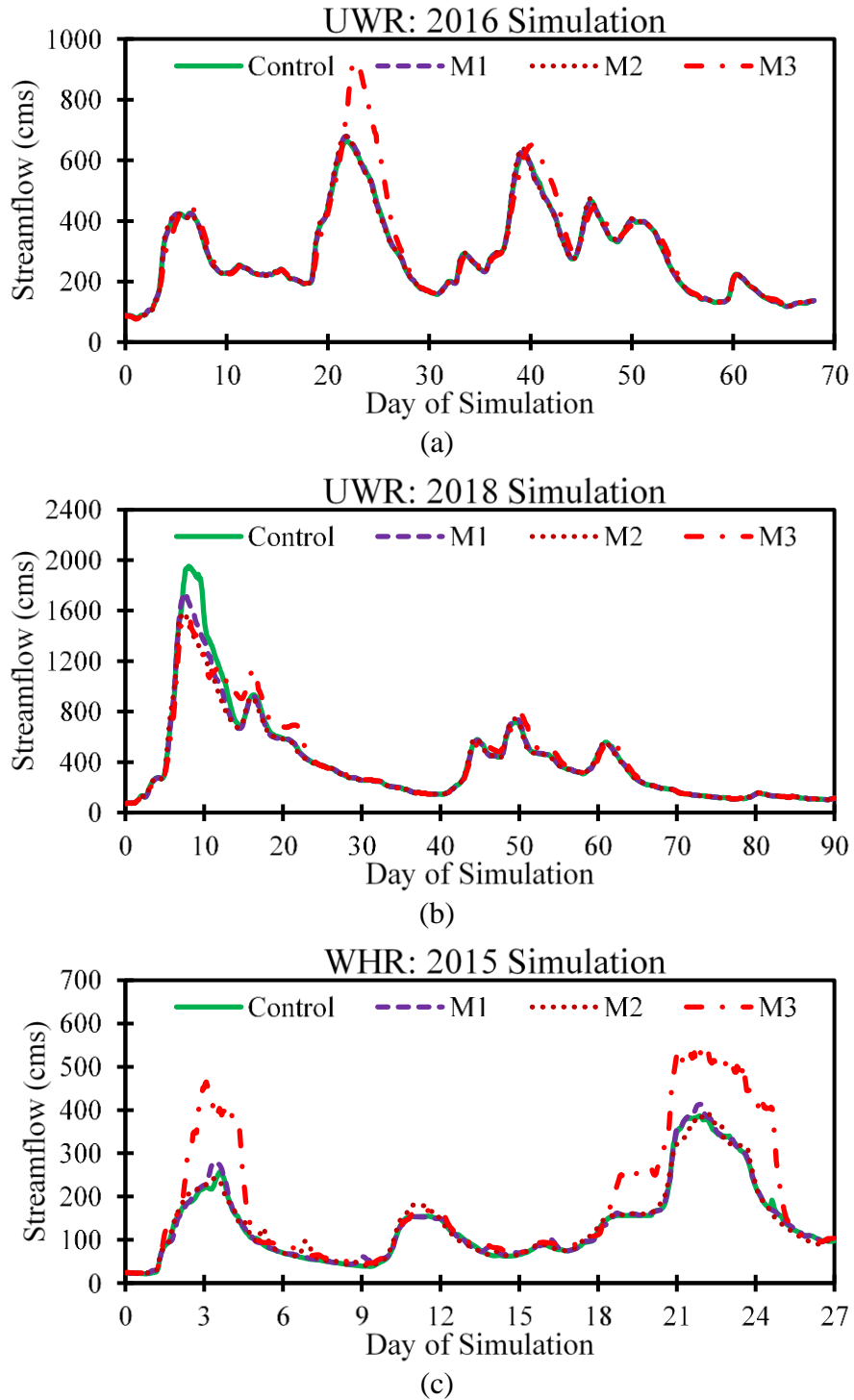
482 **Table 6:** Performance metrics comparing the inundation area and outlet hydrographs estimated  
 483 by M1, M2 and M3 with respect to Control

Simulation	Configuration	Error in Inundation Area (%)	Hydrograph Comparison at Outlet			
			NSE	PBias (%)	RSR	Error in Peak Flow (%) <sup>*</sup>
UWR (2016)	M1	-1.62	1.00	0.22	0.03	2.46
	M2	-6.84	1.00	0.24	0.05	2.58
	M3	25.36	0.81	6.19	0.44	39.76
UWR (2018)	M1	-2.78	0.97	-3.68	0.16	-10.87
	M2	-4.41	0.94	-5.56	0.24	-19.36
	M3	-0.31	0.93	0.62	0.27	-20.98
WHR (2015)	M1	1.11	0.99	1.90	0.09	6.76
	M2	-5.11	0.98	2.04	0.13	1.73
	M3	19.37	0.02	40.43	0.99	40.37

484 <sup>\*</sup>Error in peak flow corresponds to the highest peak in the simulation period

485

486



487  
488  
489  
490

**Figure 10:** Comparison of outlet hydrographs of M1, M2 and M3 against Control of UWR for (a) 2016 simulation, (b) 2018 simulation and (c) WHR for 2015 simulation

491 The performance metrics (Table 6) and the outlet hydrographs (Figure 10) show that the  
492 model performance depreciates with a reduction in bathymetric detail. In all cases, there is a  
493 decrease in NSE and an increase in RSR and Error in Peak Flow as the bathymetric representation  
494 changes from M1 to M2 and M3. The difference in performance levels is highest between M2  
495 (depth information only) and M3 (no additional bathymetric detail). The addition of accurate  
496 channel conveyance in addition to depth (M1 vs M2) leads to a small but not insignificant change  
497 in performance, especially in terms of maximum inundation area. Finally, the difference between  
498 the estimates of Control and M1 is small for both inundation area and outlet hydrographs.

499 Incorporating accurate representation of thalweg elevation for M1 and M2 (with respect to  
500 Control) leads to an increase in the longitudinal slope of the river network (Table 4) as compared  
501 to M3. This increase in slope increases the flow velocities in the direction of river flow for Control,  
502 M1 and M2. Additionally, the channel conveyance capacity plays an important role in determining  
503 the volume of water that overflows the riverbanks into the floodplains as the flood wave propagates  
504 along the river network. The main river channel and the floodplains can have significantly different  
505 roughness characteristics, due to the different landuse and land cover in the watershed.

506 UWR has a higher roughness in the floodplains because its floodplains are dominated by  
507 forests, shrubs and agricultural lands which have Manning's  $n$  in the range of 0.18 – 0.24.  
508 Therefore, the water inundating into the floodplains experiences higher frictional forces thereby  
509 reducing the flow velocity in the floodplain when compared to the water in the main channel  
510 (Manning's  $n$ : 0.035). The difference in channel conveyance capacities of M1, M2 and M3 lead to  
511 differences in the partitioning of flood wave between the main channel and the floodplains, which  
512 in turn leads to differences in the flow hydrographs at the outlet. For example, the 2016 simulation  
513 in UWR is a relatively small event where most of the water stays within the banks for Control, M1

514 and M2. However, M3's inadequate conveyance capacity leads to a higher volume of water  
515 flowing through the floodplains. Figure 10(a) shows that the peaks for M1 and M2 are similar to  
516 those of Control, whereas M3's peak is delayed by 24 hours as compared to Control (for the peak  
517 observed on 15<sup>th</sup> March 2016 (day 22)) due to slow propagation of the excess water flowing  
518 through the floodplains. In the case of WHR, 89% of the floodplains (Table 1) are developed and  
519 have a smaller roughness (Manning's  $n$ : 0.011 – 0.015). A higher percentage of developed  
520 (impervious) region causes the rainfall-induced surface runoff to travel through the floodplain  
521 faster before reaching the river channels, thereby, resulting in increased flow at the outlet as shown  
522 in Figure 10(c).

523 It is expected that the configuration with higher bathymetric detail should perform better  
524 and that the performance should reduce with decreasing levels of bathymetric detail. However, for  
525 small within-channel events (< 2-year return periods) such as those in the 2016 simulation at UWR  
526 and the 2015 simulation at WHR, the decrease in model performance from M1 to M2 is negligible  
527 as compared to the decrease in model performance from M2 to M3. The additional channel  
528 conveyance in M2 as compared to M1 (and Control) does not adversely affect model performance  
529 since most of the flow is confined to the channel and the volume of water flowing through the  
530 floodplains is minimal. For medium-sized events (> 2-year events but < 25-year event) such as the  
531 2018 event in UWR, the partitioning of water becomes more important and both overestimated  
532 (M2) and underestimated (M3) channel conveyance leads to poorer model performance. For  
533 example, the RSR (Table 6) is 0.24 and 0.27 for M2 and M3, respectively while M1 has a better  
534 RSR of 0.16. In the case of events with much higher magnitude of streamflow (>50-year return  
535 period), the impact of additional channel conveyance and increased slope is less significant as the  
536 proportion of water in the main channel is relatively small when compared to the floodplains.

537 Therefore, for high magnitude flow, it can be argued that the difference in the volume of water  
538 routed through the floodplains for different configurations becomes insignificant resulting in  
539 similar model performance.

540 In terms of maximum inundation extent, estimates of M1 are close to those of Control. M2  
541 has a higher channel conveyance capacity than Control which leads to a smaller inundation area  
542 whereas M3 has a smaller channel conveyance capacity than Control leading to an overestimation  
543 in the maximum inundation area. This behavior is consistent with previous findings on the effect  
544 of bathymetry on inundation extent (Dey et al., 2019; Grimaldi et al., 2018). One notable exception  
545 is M3 for 2018 simulation in UWR, where the overestimation in inundation area due to low channel  
546 conveyance capacity is countered by the lower peak in outlet hydrograph leading to similar  
547 inundation area estimates for M3 and Control.

548 Overall, the results indicate that depth (slope) and channel conveyance (cross-sectional  
549 area), irrespective of the shape, act as important controls for overland flow especially for medium-  
550 sized events and that the error due to overestimating channel conveyance reduces for small within  
551 bank events. Typically, hydrologic and hydrodynamic model parameters are calibrated against  
552 observed hydrographs at gauged locations. In the absence of bathymetry and adequate model  
553 physicality, such calibration would have resulted in the lack of channel storage in the river network  
554 being compensated by parameter values that characterize other physical processes. For example,  
555 in the absence of river bathymetry, an alternate approach is to assume simplified cross-sectional  
556 shapes to develop a hydrodynamic model and calibrate the depth of these cross-sections and the  
557 roughness characterization in the hydrodynamic model using observed hydrographs, stage or  
558 rating curves (Gichamo et al., 2012; Grimaldi et al., 2018; Neal et al., 2015; Price, 2009). Such an  
559 approach will not account for the effect of river bathymetry (depth) on streamflow generation

560 processes such as infiltration and lateral seepage. Instead, the calibrated values of depth and  
 561 roughness try to compensate for the inaccurate representation of fluvial processes which may lead  
 562 to additional error in the model when simulating different events. To further investigate these  
 563 issues, the subsequent sections compare the estimates of infiltration, lateral seepage, backwater  
 564 flow and inundation area between different bathymetric configurations. This will determine if the  
 565 difference in watershed response to bathymetric representations is limited to surface routing only  
 566 or if its effect extends to other fluvial processes such as SW-GW interactions.

#### 567 *6.4 Effect on Infiltration*

568 Results, presented in Figure 11 and Table 7, show that difference in infiltration rates  
 569 estimated by M3 with respect to Control is the highest, followed by M2 and M1 which indicate  
 570 that increasing bathymetric detail also improves the estimation of daily infiltration rates. M3's  
 571 performance is particularly poor which is reflected in the negative and near-zero NSE values. The  
 572 estimates of daily infiltration rate improve drastically from M3 to M2, with a relatively smaller  
 573 improvement from M2 to M1 as indicated by the increasing values of NSE and decreasing values  
 574 of RSR (Table 7), which is similar to the behavior of SW fluxes during a flood event (Section 6.3).

575 **Table 7.** Performance metrics comparing the daily infiltration rates in the floodplain estimated  
 576 by M1, M2 and M3 with respect to Control

Simulation	Configuration	NSE	Pbias (%)	RSR	Error in Peak (%) <sup>*</sup>
UWR (2016)	M1	0.98	-2.2	0.14	-5.24
	M2	0.86	-8.9	0.38	5.94
	M3	-3.19	59.3	2.03	74.14
UWR (2018)	M1	0.86	-14.8	0.37	-11.95
	M2	0.71	-22.0	0.54	-14.51
	M3	0.02	37.3	0.98	14.26
WHR (2015)	M1	0.84	1.6	0.39	21.96
	M2	0.47	-7.3	0.71	20.75
	M3	-0.40	23.5	1.16	35.70

577 <sup>\*</sup>Error in peak corresponds to the highest peak in the simulation period

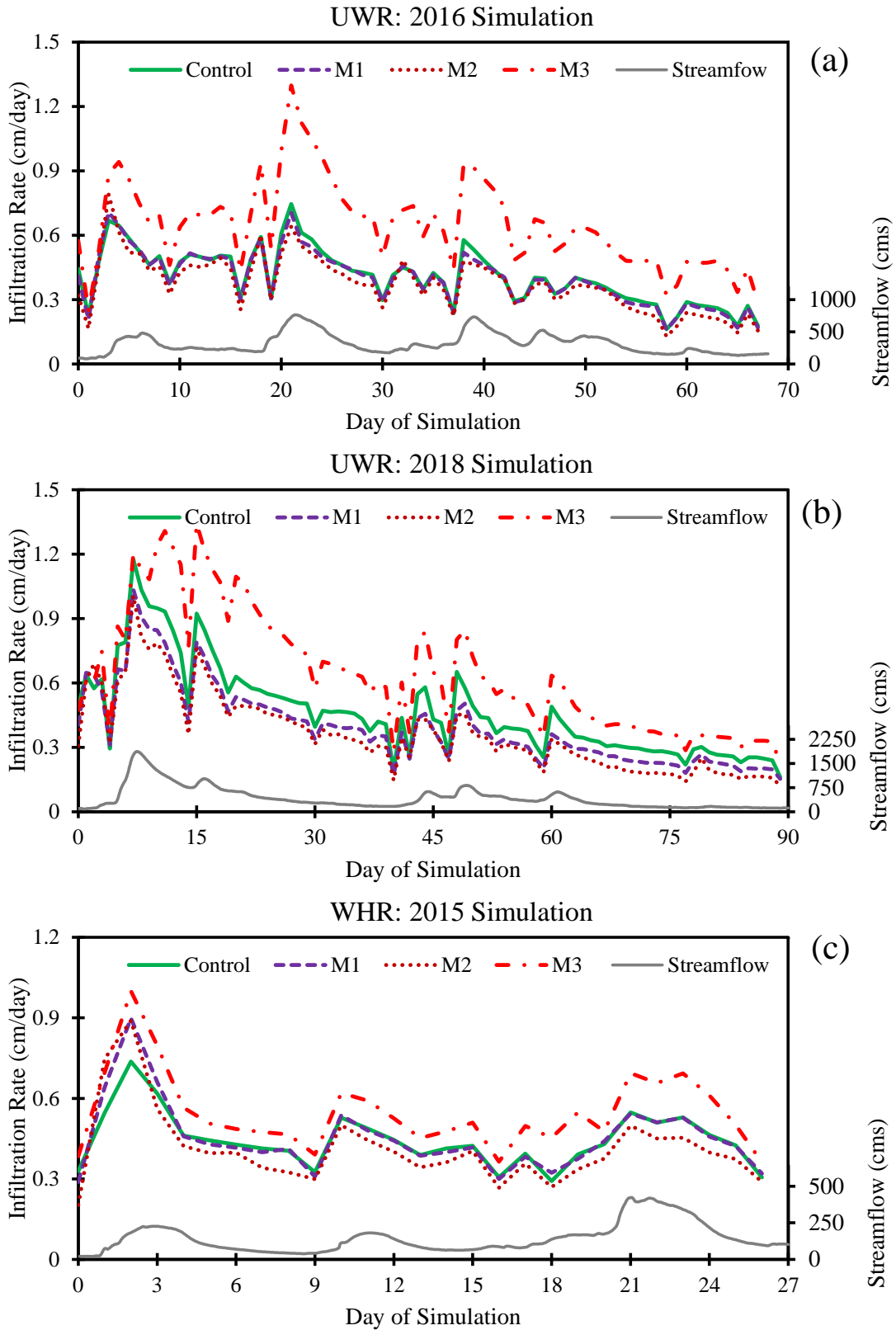


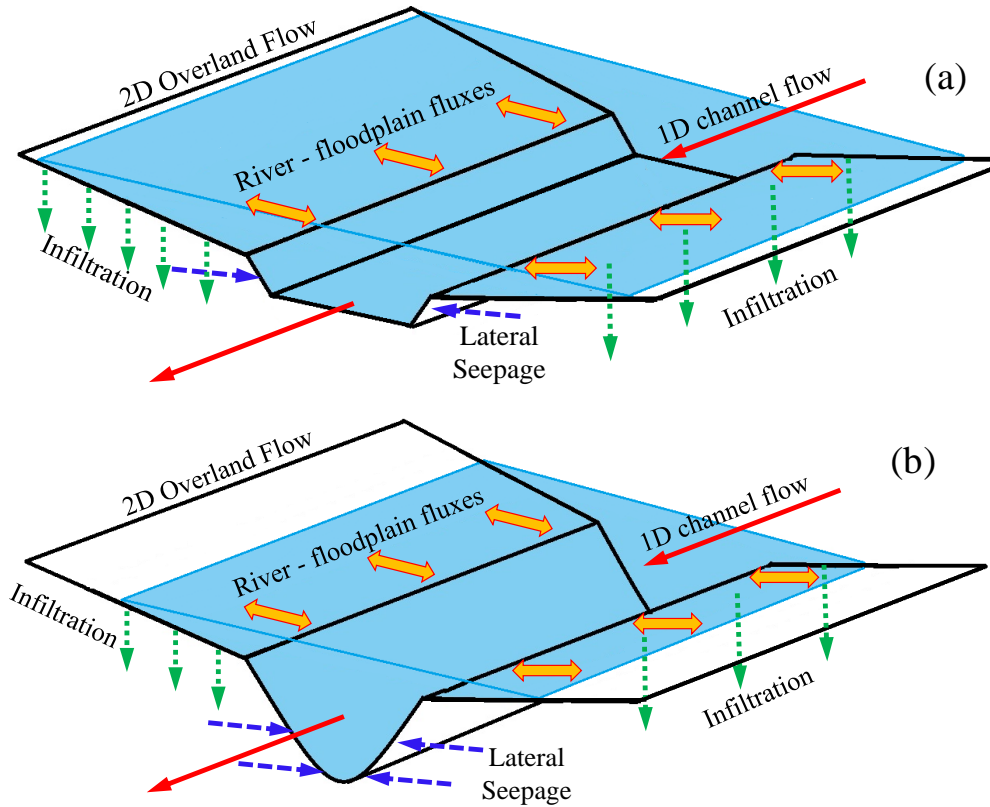
**Figure 11:** Daily infiltration rate in the floodplains of UWR for (a) 2016 simulation, (b) 2018 simulation and (c) WHR for 2015 simulation. The observed outlet hydrograph is shown in grey line on secondary axis.

578  
579  
580  
581

582

583           Initially, as seen in Figure 11, the infiltration rates are similar for all configurations because  
584 the flow is confined to the saturated river channels. As the flood waves travel through the stream  
585 network, the lateral SW flux from the river channels to the floodplains increases. As demonstrated  
586 using a conceptual diagram in Figure 12, the SW flux into the floodplains is controlled by the  
587 channel conveyance capacity of the river network. High conveyance capacity not only leads to  
588 lower floodplain storage but also reduces the total volume of water available for infiltration into  
589 the subsurface leading to lower rates of infiltration and vice-versa. This effect can be seen in all  
590 three events, where M3 (lower channel conveyance capacity) is consistently overestimating the  
591 infiltration rate whereas M2 (higher channel conveyance capacity) is consistently underestimating  
592 the infiltration rates with respect to Control. M1 has a similar channel conveyance capacity to  
593 Control and is performing the best as evident from its high NSE.

594           Further, once the flood wave starts receding, the SW fluxes recede from the floodplain  
595 back into the river channels. In this case, higher channel conveyance allows the water to recede  
596 faster from the floodplains leading to smaller residence times for surface water in the floodplains  
597 which further maintains the difference in the total infiltration volume even in the receding part of  
598 the flood event. This effect can be seen in Figure 11(b) where there are differences between the  
599 infiltration rates of the three configurations from Control even after the flood wave recedes, for  
600 example, between Day 30 (24<sup>th</sup> March 2016) and Day 36 (30<sup>th</sup> March 2016) for the 2016 event and  
601 between Day 25 (12<sup>th</sup> March 2018) and Day 35 (22<sup>nd</sup> March 2018) for the 2018 event in UWR.



602  
603  
604  
605  
606  
607  
608

**Figure 12.** Conceptual figure illustrating the difference in physical processes between two bathymetric configurations with (a) low and (b) high channel conveyance capacities. Low channel conveyance capacity leads to a higher inundation area, WSE and infiltration and lower lateral seepage as compared to a bathymetric configuration with higher channel conveyance capacity.

609  
610  
611  
612  
613  
614  
615  
616  
617

In case of WHR (Figure 11(c)), the infiltration rates estimated by M1, M2 and M3 exhibit a similar trend to that of UWR – M1 is closest to Control with M2 underestimating the infiltration rate and M3 overestimating the infiltration rate. However, the difference between the estimates produced by the different bathymetric configurations is smaller for WHR when compared to UWR. This variation in WHR can be attributed to the different landuse patterns in the floodplains of WHR. There is a higher percentage of developed area in the floodplains (Table 1) of WHR leading to a lower available subsurface storage and lower infiltration capacity in the floodplains. Additionally, the water flows faster through the floodplains because of the lower roughness in developed regions allowing the water in the floodplains to recede faster into the main channel after

618 the flood peak passes through the river network. These two factors together lead to a smaller  
619 difference between the estimates of the different bathymetric configurations in case of WHR than  
620 in UWR.

621 It is evident that the effect of improper bathymetric representation is not limited to SW  
622 processes but also affects SW-GW interactions such as infiltration which can, in turn, affect the  
623 rainfall-runoff in a watershed since there is bi-directional feedback between these two processes.  
624 However, loosely coupled hydrologic and hydrodynamic models (Afshari et al., 2018; Follum et  
625 al., 2020; Rajib et al., 2020; Wing et al., 2017) neglect such feedbacks which may get compounded  
626 by improper bathymetric representation. Errors in bathymetric representation combined with  
627 simplistic routing procedure in the hydrologic model may lead to erroneous estimates of infiltration  
628 and streamflow which can propagate through the hydrodynamic model.

### 629 *6.5 Effect on Lateral Seepage*

630 The net lateral seepage is calculated as the difference in cumulative lateral seepage inflow  
631 and outflow for each day of the simulation. As such, a negative lateral seepage indicates that the  
632 river network is losing water into the subsurface, whereas a positive lateral seepage indicates that  
633 the river network is gaining water from the subsurface.

634 As shown in Figure 13, the net lateral seepage is negative during the flood event as a large  
635 volume of water seeps into the subsurface due to higher heads in the river channels. However, after  
636 the flood wave recedes, the net lateral seepage becomes positive as the water that has seeped into  
637 the subsurface during the event starts recharging into the river channels. M1 provides decent  
638 estimates of lateral seepage rate when compared to Control, as is evident from high NSE, low RSR  
639 and low error in peak lateral seepage rate. M2's performance is even worse than M3's. It has a

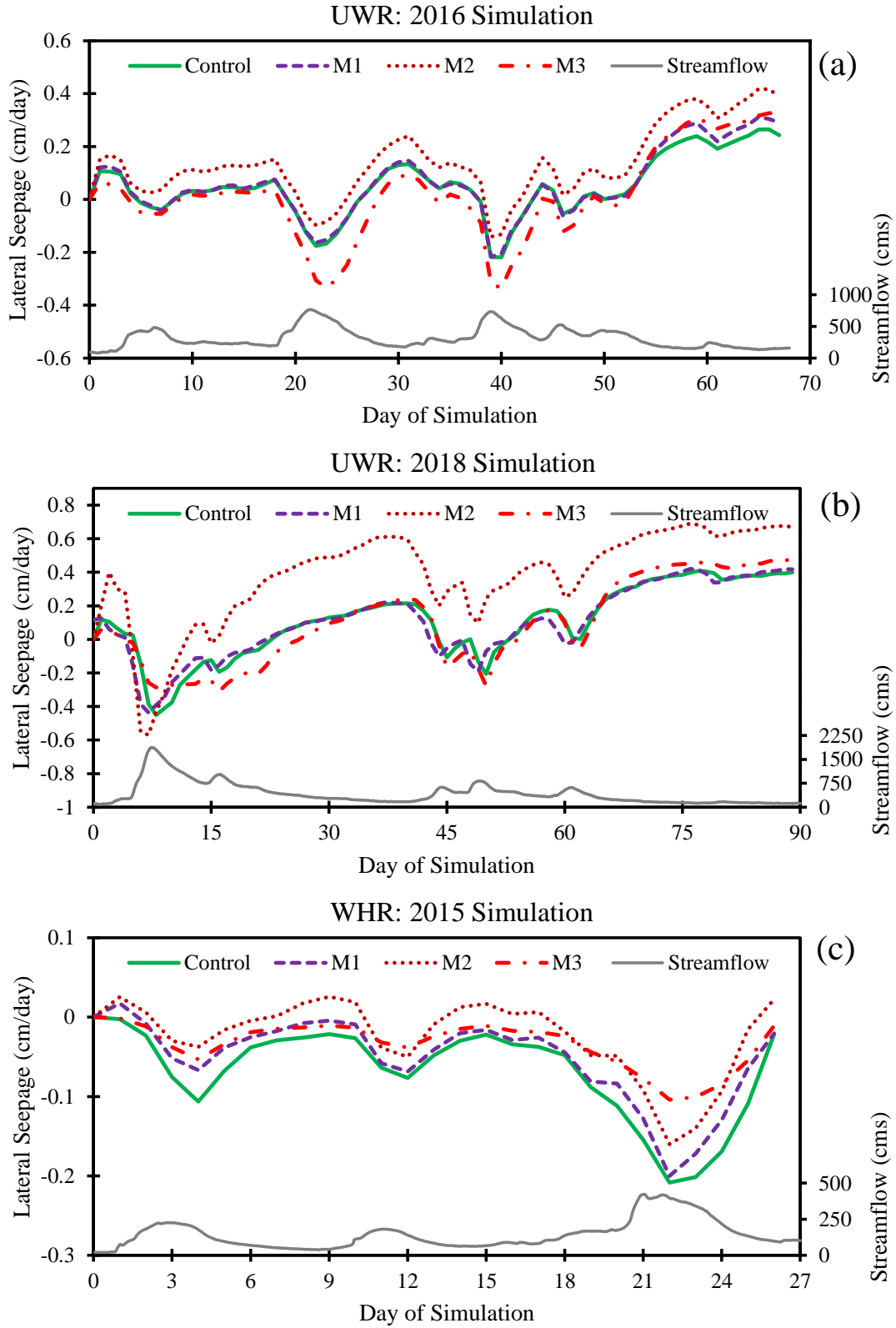
640 negative NSE for the 2018 event in UWR and exhibits large biases in the positive direction for all  
 641 three events.

642 **Table 8.** Performance metrics comparing the daily net lateral seepage rate in the floodplain  
 643 estimated by M1, M2 and M3 with respect to Control

Simulation	Configuration	NSE	Pbias (%)	RSR	Error in Peak (%) <sup>*</sup>
UWR (2016)	M1	0.97	20.8	0.16	17.44
	M2	0.32	183.0	0.82	57.83
	M3	0.61	-69.8	0.62	26.71
UWR (2018)	M1	0.99	-7.2	0.10	-3.13
	M2	-1.01	258.6	1.41	53.39
	M3	0.90	-6.1	0.32	5.70
WHR (2015)	M1	0.87	-24.3	0.35	-3.91
	M2	0.30	-65.0	0.82	-23.10
	M3	0.40	-50.0	0.76	-50.00

644 <sup>\*</sup>Error in peak corresponds to the highest peak in the simulation period

645



646

647

648

649

**Figure 13:** Daily lateral seepage rate in the floodplains of UWR for (a) 2016 simulation, (b) 2018 simulation and (c) WHR for 2015 simulation. The observed outlet hydrograph is shown in grey line on secondary axis.

650           The lateral seepage is controlled by the saturated area available for the exchange of fluxes  
651 between the river channel and GW and the head distribution in the channel and floodplains. As the  
652 flood wave propagates along the channel network, it pushes the old water in the channel as well  
653 as the GW in the floodplains away from the river channel. Similarly, as the water in the channel  
654 recedes, it creates a pulling effect that forces water from the surrounding GW in the floodplains to  
655 rush to the river channel. This leads to a high correlation between GWT elevation in the river  
656 channel and river channel heads (Jung et al., 2004). The WSE in the river channel is governed by  
657 both the volume of water flowing through the channel and the channel geometry (bathymetry).  
658 The overall channel bed elevations for M2 are lower than that of Control. It also has the highest  
659 channel conveyance capacity. WSE in the channel is lowest for M2, followed by those of Control  
660 and M1 and finally, M3 has the highest WSE. Lower the WSE in the channel, lower the SW head  
661 in the channel driving the lateral seepage. This leads to a less negative (more positive) lateral  
662 seepage rate for M2. This also explains the more negative estimates of M3 which has the lowest  
663 channel conveyance capacity and highest WSE of the three configurations. A similar scenario is  
664 observed for WHR, but a smaller difference in net lateral seepage is observed between the different  
665 bathymetric configurations due to WHR having a primarily developed landuse leading to limited  
666 SW-GW interactions.

667           The saturated surface area in the river network (wetted perimeter in a cross-section)  
668 available for SW-GW exchange also plays a role in controlling the lateral seepage. M1 and M2  
669 have the same surface area but different channel conveyance capacity leading to significantly  
670 different performance in terms of lateral seepage rates. Also, as shown in Table 3, the difference  
671 in surface areas between the configurations is not as high as the difference between channel  
672 conveyance capacity. This indicates that incorporating channel geometry with accurate channel

673 conveyance capacity may suffice in accurately capturing the SW-GW processes for medium to  
 674 large watersheds.

675 In this study, Control incorporates the thalweg variability along a river network leading to  
 676 better representation of thalweg-gegenweg and side slopes as recommended by Chow et al., (2018)  
 677 and Doble et al., (2012), respectively to model the lateral seepage. The differences between  
 678 estimates of Control and M1 (vertical side slopes and symmetric river channel geometry) are  
 679 relatively small which indicates that these two bathymetric characteristics play a minor role in  
 680 lateral seepage across large river networks. More importantly, the stark difference in the  
 681 performance of M1 and M2 relative to Control indicates that channel conveyance capacity has a  
 682 greater effect on the SW-GW fluxes at larger spatial domains incorporating river corridor or river  
 683 networks (and beyond).

#### 684 *6.6 Effect on Groundwater Table*

685 As shown in the previous sections, the incorporation of river bathymetry, specifically the  
 686 channel conveyance, has a significant impact on subsurface processes such as infiltration and  
 687 lateral seepage. Since both these processes are related to available subsurface storage, which is  
 688 subsequently dependent on the water table depth, the effect of incorporating bathymetry on GWT  
 689 elevation is analyzed in this section by comparing the maximum GWT elevation estimated by the  
 690 three configurations with Control as shown in 13. The differences in maximum GWT elevations  
 691 ( $\Delta GWT_{max}$ ) has been corrected for biases due to initial conditions as per the following equation  
 692 (Equation 5).

$$693 \quad \Delta GWT_{max,Mi} = GWT_{Control,max} - GWT_{Mi,max} - (GWT_{Control,initial} - GWT_{Mi,initial})$$

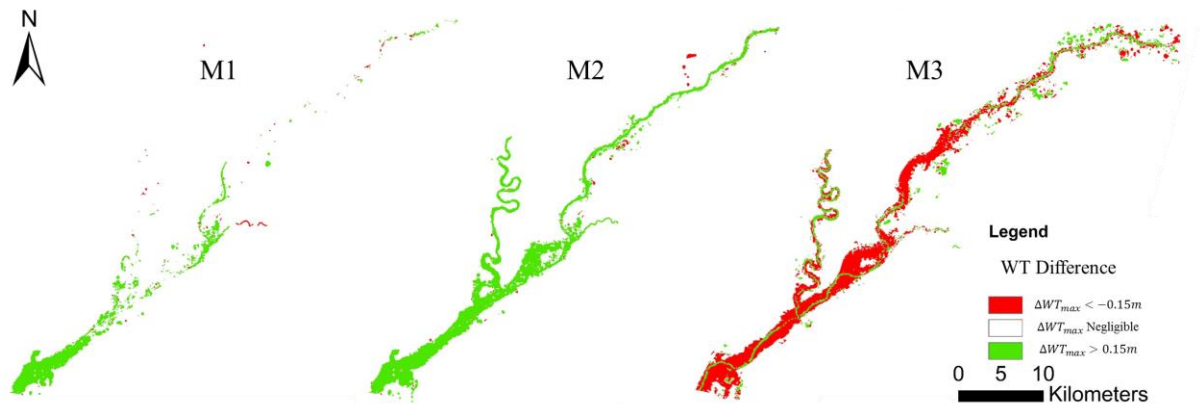
694 (Equation 5)

695 where  $\Delta GWT_{max,Mi}$  is the bias-corrected difference in maximum water table elevations  
696 estimated by the bathymetric configuration  $Mi$  (M1, M2 or M3) and Control, and  
697  $GWT_{Control,initial}$  and  $GWT_{Mi,initial}$  are the initial water table elevations for Control and  $Mi$  (M1,  
698 M2 or M3) respectively. Areas with a positive value of  $\Delta GWT_{max,Mi}$  for a given configuration  
699 have a higher change in water table elevation for Control as compared to that configuration while  
700 negative values of  $\Delta GWT_{max,Mi}$  indicate that the region has a higher change in water table  
701 elevation for that configuration compared to Control. If  $|\Delta GWT_{max,Mi}| < threshold$ , then that  
702 region is said to have no meaningful difference in the maximum water table elevations estimated  
703 by M1 and M2. The *threshold* is implemented for filtering out small differences caused due to  
704 model discretization and conversion between unstructured mesh and gridded data. In this study,  
705 the *threshold* is set to 0.15m (6 inches) – an arbitrarily chosen value based on prior modeling  
706 experience. Since the only difference in the different configurations is the bathymetric  
707 representation, analyzing  $\Delta GWT_{max}$  across the study area demonstrates the spatial distribution of  
708 the effect of river bathymetry on GW processes.

709 Figure 14 shows the areas in UWR where the maximum water table elevations are  
710 significantly different for the three configurations compared to Control for the 2018 simulation.  
711 M1 has the least differences in  $\Delta GWT_{max}$  compared to M2 and M3 as evident with a lesser  
712 percentage of green and red zones in Figure 14. M2 and M3 have contrasting distributions of  
713  $\Delta GWT_{max}$  in the floodplains. M2 has a higher percentage of areas with positive  $\Delta GWT_{max}$   
714 whereas M3 has a higher percentage of negative  $\Delta GWT_{max}$  in the floodplains with the positive  
715  $\Delta GWT_{max}$  mostly confined to the main river channel. This difference in the distribution of  
716  $\Delta GWT_{max}$  for M2 and M3 can be attributed to differences in infiltration and lateral seepage rates  
717 of M2 and M3 (Section 6.4 and 6.5). The infiltration rate of M2 is lower than Control which means

718 M2 has a lower volume of water infiltrating into the GW leading to lower changes in GWT  
 719 elevation as compared to Control leading to positive  $\Delta GW T_{max}$ . On the other hand, M3 has a  
 720 higher infiltration rate than Control leading to higher changes in GWT with respect to Control  
 721 leading to negative  $\Delta GW T_{max}$ . The difference in lateral seepage also further enhances the  
 722 difference between Control and M2 or M3. M2 has a more positive lateral seepage which indicates  
 723 that the river channel is gaining more (losing less) water from the GW, leading to smaller changes  
 724 in GWT whereas M3 has a more negative lateral seepage indicating the stream losing more water,  
 725 which causes higher changes in GWT in the floodplains. However, the volume of water being  
 726 lost/gained due to lateral seepage is small as compared to the volume of water being gained through  
 727 infiltration.

728



729

730 **Figure 14.** Figure showing the spatial distribution of differences between change in water table  
 731 elevations estimated by the different bathymetric configurations and Control at Wabash River  
 732 Basin (UWR). Green regions have a positive  $\Delta WT_{max}$  which indicates that those regions have  
 733 lower changes in water table elevation from initial water table elevations for a given bathymetric  
 734 configuration as compared to Control, and vice-versa for the red regions.

735

736 The spatial distribution of  $\Delta GW T_{max}$  also highlight the fact that the effect of bathymetric  
 737 configuration on GWT is spread throughout the network and is not limited to the main stem of the  
 738 river. Additionally, it highlights the fact that there is a need for incorporating the channel

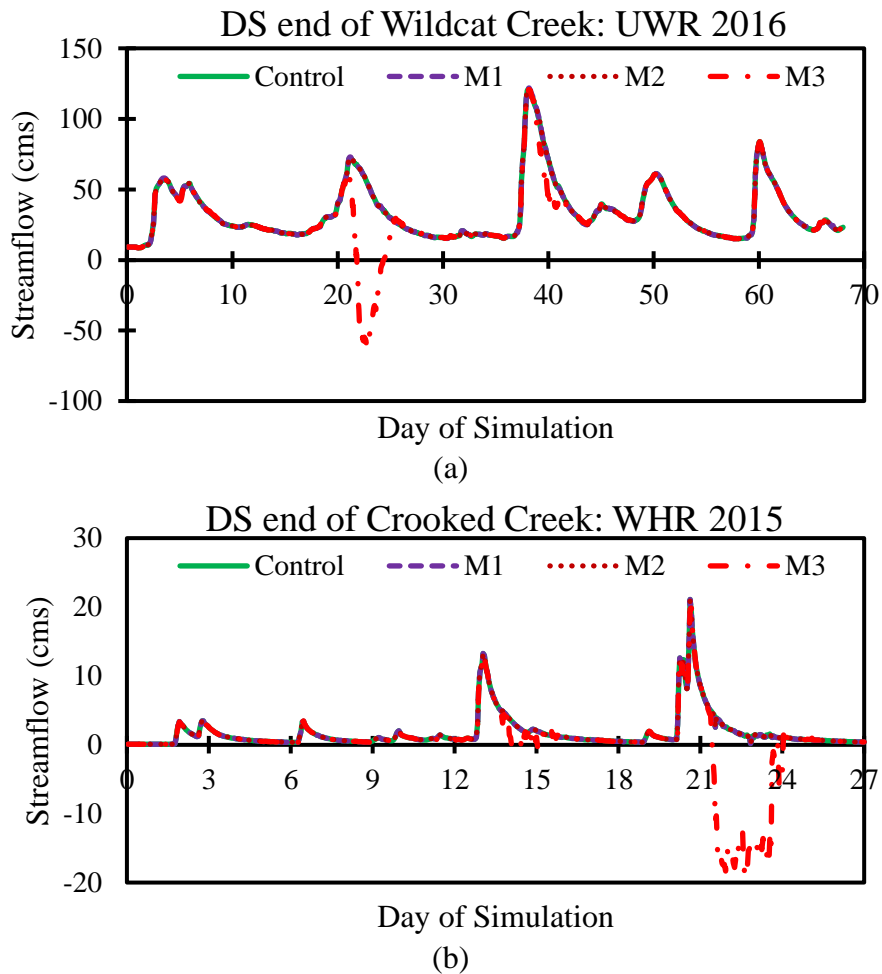
739 conveyance capacity accurately since both underestimation (M3) and overestimation (M2) of  
740 channel conveyance capacity leads to significant differences in estimates of GWT elevation. This  
741 may be particularly relevant in the field of contaminant transport, wetland modeling and stream  
742 restoration (Banks et al., 2011; Cienciala and Pasternack, 2017; Czuba et al., 2019; Osman and  
743 Bruen, 2002).

744 Traditional hydrodynamic modeling cannot reflect the change in flow volume due to  
745 within-reach hydrologic processes. Therefore, hydrodynamic models have only been able to  
746 highlight the effect of poor bathymetric representation on SW fluxes. However, flooding-related  
747 physical processes are codependent on each other; they continuously influence each other directly  
748 or indirectly through feedback loops. The results presented in this study show that the impact of  
749 bathymetry is not limited to surface fluxes but also extends to subsurface processes and SW-GW  
750 interactions. Effective incorporation of bathymetric representation in data-sparse regions should  
751 focus on accurately estimating bathymetric characteristics rather than on the overall shape of the  
752 channel geometry. Specifically, the focus should first be on incorporating accurate estimates of  
753 channel conveyance capacity and thalweg elevation, followed by side slopes and channel  
754 asymmetry for accurately simulating the SW-GW processes in floodplains for river networks at  
755 large spatial domains.

#### 756 *6.7 Effect on Backwater Flow at Confluence*

757 At a river confluence, the two streams draining to the confluence may not have similar  
758 thalweg elevation, especially when lower order streams meet a higher order stream. Usually, the  
759 main river is deeper than the tributary, and the difference in thalweg elevation increases as the  
760 difference in the stream orders of the main river and its tributaries increases. This difference in  
761 thalweg elevation can affect the flow patterns near a confluence but this effect is usually ignored

762 in traditional hydraulic models. To investigate this effect, the streamflow hydrograph just upstream  
 763 of the confluence is compared for M1, M2 and M3 against Control. Figure 15(a) shows the  
 764 hydrograph at the downstream end of Wildcat Creek as it drains into the Wabash River. The figure  
 765 shows that Wildcat Creek experiences backwater flow (negative flow) from the Wabash River on  
 766 days 22 to 24 of the simulation (16<sup>th</sup> March 2015 to 18<sup>th</sup> March 2015) in case of M3, whereas M1  
 767 and M2 do not exhibit this backflow – same as Control. This indicates that the backwater is  
 768 spuriously induced by the incomplete representation of bathymetry in M3.  
 769



770  
 771 **Figure 15.** Figure showing hydrographs at the downstream (DS) end of tributary at (a) the  
 772 Wildcat Creek – Wabash River confluence (UWR) and (b) the Crooked Creek – White River  
 773 confluence (WHR) for all three configurations.

774

775 All three configurations (M1, M2 and M3) have differences in bathymetric characteristics.  
776 M3 is based on the original Lidar where the entire river network is characterized by a flat surface  
777 with a very mild longitudinal slope. The thalweg elevations are the same for Control, M1 and M2  
778 but are different from those of M3. The fact that only M3 is exhibiting such a behavior can be  
779 attributed to the difference (or lack thereof) in thalweg elevation of the main stem and the tributary.  
780 In case of Control, M1 and M2, the thalweg is higher for Wildcat Creek (155.7 m) as compared to  
781 Wabash River (154.8 m) at the confluence, which acts as a barrier to the flow of water from  
782 Wabash River to Wildcat Creek, thereby reducing the backwater flow in the channel. This  
783 elevation difference between Wabash River and Wildcat Creek is not present in M3 where the  
784 thalweg elevation for both the channels is 156.2 m. This allows the water from the Wabash River  
785 to travel upstream along Wildcat Creek, thereby leading to backwater flow. A similar effect can  
786 also be observed in WHR at the confluence of Crooked Creek and White River, as demonstrated  
787 by Figure 15(b) where Control, M1 and M2 have a difference of 0.7 m in the thalweg of Crooked  
788 Creek and White River at the confluence but M3 has no difference in thalweg elevation at the  
789 confluence.

790 This difference in flow patterns is not observed at every confluence. For example, the  
791 difference in flow at the downstream end of the Tippecanoe River (just upstream of the Wabash-  
792 Tippecanoe confluence) is negligible. The Wabash River – Tippecanoe River confluence has a  
793 smaller difference in thalweg elevation at the confluence (0.5m) than the Wabash River – Wildcat  
794 Creek confluence (0.9 m). Figure 15 also shows that the backwater flow exists for only one of the  
795 peaks at the Wabash River – Wildcat Creek confluence. This difference in behavior can be  
796 explained by the relative difference in magnitude of flow along the tributary and the main channel.

797 Surface routing of water is governed by the total head of water, which in turn, depends on the  
798 thalweg elevation and water depth. The water depth depends on the volume of water flowing  
799 through the channel. If the flood wave traveling along a tributary is comparable to the flood wave  
800 of the main river at the confluence, the flood wave in the tributary may act as a further barrier to  
801 backwater flow. This may compensate for the lack of difference in thalweg elevation in M3 and  
802 impede backwater flow. Therefore, the relative size of the channels meeting at a confluence and  
803 the difference in flow through them may be responsible for the backwater effect to be important at  
804 confluences.

805         If two streams at a confluence have a large difference in thalweg elevations of main channel  
806 and tributary or the events are of different magnitudes, the absence of bathymetry at confluences  
807 can result in highly erroneous streamflow at the watershed outlet due to backwater flow. The  
808 spurious backwater flow in the absence of bathymetry can lead to erroneous localized flooding  
809 around the confluence. Therefore, confluence geometry with appropriate representation of  
810 differences in thalweg elevations between the tributary and main river at the confluence must be  
811 incorporated to ensure accurate hydrodynamic connectivity along the river network, particularly  
812 for large-scale applications spanning large networks which have confluence between rivers with  
813 markedly different bed elevations (Mejia and Reed, 2011; Tran et al., 2020; Trigg et al., 2009).

## 814 **7. Summary and Conclusion**

815         Bathymetry is critical for accurate modeling of fluvial systems. However, traditional river  
816 modeling has focused on evaluating the effect of bathymetry on surface routing processes along  
817 single reaches, usually the main stem of the river network. Fluvial systems comprise of co-  
818 dependent surface and subsurface physical processes which affect hydrodynamic variables  
819 significantly, especially at large watershed scales. This study evaluates if the effect of river

820 bathymetry extends beyond surface processes to subsurface processes such as seepage and  
821 infiltration. Additionally, the study analyzes the bathymetric characteristics that control these  
822 processes to provide insights into effective ways to incorporate bathymetry across large river  
823 networks in data-sparse regions. To answer these research questions, a conceptual bathymetric  
824 model, SPRING, which can generate bathymetry for entire river networks, is implemented on two  
825 watersheds with distinct physical characteristics (agricultural and urban). Physically-based  
826 distributed models are created for four different bathymetric configurations with successively  
827 reduced bathymetric detail: Control (highest level of detail – calibrated asymmetric cross-sections  
828 with realistic side slope), M1 (depth, channel conveyance capacity and vertical side slope), M2  
829 (depth and vertical side slope) and M3 (original Lidar with no additional bathymetric detail).  
830 Analysis of hydrologic and hydrodynamic outputs from the four configurations leads to the  
831 following conclusions:

832       1) The application of SPRING in the Wabash (UWR) and White River (WHR) basins  
833 demonstrate its ability to estimate bathymetry for tributaries as well as the main river stem in a  
834 river network. Additionally, it can maintain hydraulic connectivity among channels with proper  
835 representation of bathymetry at confluences. Bathymetry incorporation can lead to a significant  
836 increase in channel conveyance capacity across the river network and overall longitudinal slope of  
837 the channel but the change in the surface area remain relatively small.

838       2) A comparison of the streamflow prediction at the outlet using the four configurations  
839 indicates that depth (slope) and channel conveyance (cross-sectional area), irrespective of the  
840 shape, play an important role in accurately simulating flood events across river networks. Channel  
841 conveyance capacity controls the partitioning of the flood wave between the main channel and the  
842 floodplains. Because of a significantly different roughness distribution in the floodplain compared

843 to the main river channel, the water routed through the floodplains can either slow down or speed  
844 up (depending on the land use in the floodplain). While the absence of bathymetry leads to poor  
845 performance for all events, small events may be captured accurately by incorporating accurate  
846 channel depth (thalweg elevation) only. However, for medium-sized events, both channel  
847 conveyance and depth need to be incorporated for adequately capturing the watershed response.

848 3) The impact of bathymetry on subsurface processes is demonstrated by the difference in  
849 infiltration rates across the four configurations. The infiltration rates remain similar when the  
850 channel conveyance capacity and depth are adequately incorporated. In the absence of adequate  
851 bathymetric detail, lower (higher) channel conveyance capacity causes higher (lower) influx of  
852 water into the floodplain during flood events, which increases (decreases) the floodplain residence  
853 time, thereby increasing (decreasing) the infiltration. The influence of bathymetry in infiltration is  
854 also affected by the landuse of floodplains, with developed regions showing lesser but still  
855 significant differences in infiltration.

856 4) Lateral seepage depends on the head distribution in the river network and the saturated  
857 area available for SW – GW interaction. A higher channel conveyance capacity lowers the water  
858 surface elevation and may increase the wetted area in the river network. Therefore, it leads to  
859 increased seepage from the GW into the channel, and its underestimation leads to overestimation  
860 in seepage from the channel into the GW. Lateral seepage is particularly sensitive to bathymetric  
861 detail as the result demonstrated that incorporating inaccurate channel conveyance can lead to even  
862 poorer estimates of lateral seepage as compared to not incorporating any bathymetric information.

863 5) The differences in infiltration and lateral seepage rates due to bathymetric configurations  
864 contribute to significant differences in water table elevations throughout the river network. Lack  
865 of bathymetry, especially underrepresenting the channel conveyance capacity can lead to

866 overestimation in water table elevations and vice-versa. This indicates that errors in bathymetry  
867 can propagate to surface and subsurface processes as well as the interaction between these  
868 processes.

869         6) The overall performance of the bathymetric configurations across both watersheds  
870 indicate that channel conveyance capacity and thalweg elevation (longitudinal slope) play a critical  
871 role in accurately capturing both surface and subsurface processes in H&H models. Therefore, in  
872 estimating conceptual bathymetry for data sparse regions, the focus should be on incorporating  
873 accurate channel conveyance and thalweg elevation. Additional information regarding channel  
874 side slope and channel asymmetry may further improve the accuracy of H&H model.

875         7) The bathymetry at river confluences plays a critical role in determining the flow patterns  
876 in the region. In the absence of bathymetry, the tributary may experience significant backwater  
877 flow. After bathymetry incorporation, the thalweg elevations of the main channel and tributary just  
878 upstream of the confluence may be significantly different. This acts as a barrier to backwater flow  
879 from the main channel moving upstream of the tributary. This effect seems to be localized to the  
880 vicinity of the confluences and the extent of backwater flow also depends on the relative size and  
881 timing of the flood wave arriving at the confluence from the tributary and main river.

## 882 **8. Limitation and Future Work**

883         This study demonstrates the effect of incorporating bathymetry across large river networks  
884 on watershed processes using physically-based distributed modeling. There are certain limitations  
885 to the results presented here. While the proposed framework for generating bathymetry (SPRING)  
886 can be applied to every reach including lower-order streams, this study only analyzes the effect on  
887 the main stem and three of its major tributaries at both sites. This is primarily due to the lack of  
888 accurate thalweg elevations and channel volumes across the river network. Since accurate depth

889 and channel volume are critical to generating accurate bathymetry, future studies should focus on  
890 estimating these bathymetric characteristics for all channels in a network. In this regard, remote  
891 sensing-based methods such as the FREEBIRD algorithm, hydraulic modeling based  
892 depth/volume calibration, or remote sensing-based at-a-station equations may be particularly  
893 useful (Grimaldi et al., 2018; Legleiter et al., 2011; Price, 2009). Additionally, implementing  
894 SPRING for large-scale application across river networks spanning hundreds or even thousands of  
895 kilometers requires the automated generation of input datasets such as river centerline and banks.  
896 While public datasets such as the National Hydrography Database (NHD) do exist, they suffer  
897 from inaccurate spatial correspondence with the DEM. Such large-scale implementation  
898 necessitates the use of high-performance computing and parallelization. Therefore, future work  
899 also includes developing an automated and efficient algorithm that can create these input datasets  
900 for SPRING and use parallelization methods for computational efficiency at large scales.  
901 Additionally, large-scale application of SPRING also requires evaluation of the data requirements  
902 of calibrating the parameters of SPRING as well as spatial transferability of the parameter set  
903 across different river networks.

904         The results presented here indicate that the difference due to bathymetry incorporation may  
905 be dependent on the scale of the main river, its tributaries, the magnitude and intensity of the event,  
906 and overall spatial extent and landuse distribution of the watershed. Future forays in this direction  
907 should consider researching the appropriate spatial scales at which the impact of bathymetry  
908 becomes more or less significant in the context of hydrologic and hydraulic processes. This may  
909 provide insights into when and where bathymetry incorporation is necessary and if there exist  
910 circumstances where bathymetry incorporation may be neglected for certain streams. This is  
911 particularly important in the context of developing large-scale accurate flood models.

912 **Acknowledgments and Data**

913           This work was performed with funding from the U.S. National Science Foundation (Grants  
914 1706612, 1737633, 1835822). Any opinions, findings, and conclusions or recommendations  
915 expressed in this material are those of the authors and do not necessarily reflect the views of the  
916 National Science Foundation.

917           SPRING is available for implementation as an ArcGIS toolbar. The installer and instruction  
918 manual           are           shared           in           HydroShare           at:  
919 <https://www.hydroshare.org/resource/5f997ec440ea41859bc329ea4a5d7289/>. All data used in  
920 this study will be made available in HydroShare upon acceptance of the manuscript for publication.

921

922

923 ***Appendix A1: Estimating river bathymetry at individual reaches***

924 This section gives a brief explanation of the procedure followed by SPRING to estimate  
925 river geometry for individual reaches. For more details, please refer to Dey, (2016) or Merwade,  
926 (2004).

927 For each river reach in the network, the channel centerline is divided into small segments,  
928 which are 10-14 times the width of the channel. The depth at each of these segments is estimated  
929 by linearly interpolating between the known depth at the USGS gage locations within the river  
930 network. For each segment, a normalized cross-section is created which has unit width and unit  
931 depth. First, the radius of curvature ( $r$ ) of the centerline segment is estimated using the three-point  
932 arc method. Then the width of the channel ( $w$ ) is calculated by measuring the average distance  
933 between the banks for that centerline segment. The thalweg position ( $t$ ), which is the distance of  
934 the thalweg from the channel centerline along a river cross-section, is determined using an  
935 exponential function relating the normalized radius of curvature ( $r^* = r/w$ ) to normalized  
936 thalweg position ( $t^* = t/w$ ) as shown in Equation 1. The sign of the thalweg position (left of  
937 centerline: negative, right of centerline: positive) is determined by the direction in which the river  
938 meanders. If the river meanders (turns) to the left, there is more erosion on the right bank (outer  
939 bank) and more deposition on the left bank (inner bank). Consequently, the thalweg is positioned  
940 on the right side of the centerline (positive thalweg location). SPRING determines the position of  
941 the thalweg by locating the center and radius of curvature of the meander using the three-point  
942 rule. If the center of curvature of the meander is to the left of the centerline, the thalweg is located  
943 on the right side of the centerline, that is, the thalweg position is positive and vice-versa. In  
944 summary, the position of the center of curvature of the meander relative to the centerline

945 determines the sign (direction) of the thalweg position and the radius of curvature determines the  
946 distance between the centerline and the thalweg position.

947         Finally, asymmetric cross-sections having unit depth and unit width are estimated based  
948 on the thalweg position, using a linear combination of beta-functions as shown in Equation 2. The  
949 scaling parameter,  $k$ , in Equation 2 is introduced in the equation to remove the constraint of total  
950 area in a cross-section. The area under a pdf is always equal to 1, so the area under the sum of two  
951 pdfs cannot be greater than 2. However, this constraint is not applicable to a normalized river  
952 cross-section of unit width and unit depth. The introduction of scaling parameter in the equation  
953 removes the area constraint and increases the flexibility of SPRING to create cross-sections of  
954 different shapes. The parameters of SPRING can be estimated from surveyed cross-sections  
955 available for a different section of the same river or from a different river with similar  
956 characteristics as the river in question. Finally, the width and bank elevation of the river channel  
957 for that segment is estimated using the bank lines and DEM. These are used to rescale the  
958 normalized cross-section shape to actual cross-section using Equation 3. After creating cross-  
959 sections for each centerline segment using SPRING, longitudinal 3D lines (called profile lines) are  
960 drawn along the channel intersecting the cross-sections. Channel bed elevations are interpolated  
961 between the estimated cross-sections along these profile lines in a channel centered curvilinear  
962 coordinate system (Glenn et al., 2016; Merwade et al., 2006) to create a 3D mesh depicting the  
963 channel bathymetry.

964

**965 Appendix A2: Integrated Channel and Pond Routing**

966 This section provides supplementary information on the computational framework used in  
967 Integrated Channel and Pond Routing (ICPR), a physically based tightly coupled distributed model  
968 capable of simultaneously estimating flooding related surface and subsurface processes in a  
969 watershed. Information provided in this section has been adapted from Saksena et al., (2021, 2020,  
970 2019) and Streamline Technologies, (2018).

971 The basic modeling framework consists of 1D nodes and links to represent overland flow  
972 along the river network, a 2D flexible mesh for simulating surface water (SW) flow in rest of the  
973 watershed (including the floodplains), a 2D flexible mesh for modeling groundwater (GW) flow  
974 and a storage layer between the overland and groundwater meshes representing vadose zone  
975 processes. All these elements can interact with each other which allows for a single fully-integrated  
976 system of equations. Precipitation received by the overland region is partitioned between the  
977 overland region and vadose zone. The water in the overland region is routed through the overland  
978 mesh while the water that enters the soil column is stored in the vadose zone. Water from the  
979 vadose zone flows into GW from where it can either remain stored in GW, move to the overland  
980 region through seepage or return to vadose zone.

981 The river network is discretized in the form of 1D nodes which are connected by 1D links  
982 which transport water from one node to another. The links can be modified to include hydraulic  
983 structures such as weirs, culverts or bridges. The 1D river network interacts with the overland flow  
984 in the floodplains (and the rest of the watershed) through the 1D-2D interface along the channel  
985 boundary (banks). The 2D overland flow is characterized by a triangular mesh of flexible  
986 resolution also known as a triangular irregular network (TIN). The modeler ensures that all  
987 topographic features relevant to overland flow of water are adequately represented in TIN. Each

988 vertex of the TIN has a honeycomb shaped subbasin which is created by joining the midpoints of  
 989 the triangle sides to the geometric center of the triangular element in the TIN. These honeycombs  
 990 are further divided into control volumes (CV) by intersecting them with the geospatial datasets  
 991 used for parametrization. This ensures that the sub-grid variability in the geospatial datasets within  
 992 each element of the TIN is conserved. Each CV acts as a subbasin where all hydrologic  
 993 computations occur. The 2D overland flow occurs along the edges of the TIN. ICPR implements  
 994 a finite volume discretization for conservation of mass as depicted in Equations A1-A4.

995

$$996 \quad dz = \left( \frac{Q_{in} - Q_{out}}{A_{surface}} \right) dt \quad \text{(Equation A1)}$$

$$997 \quad Z_{t+dt} = Z_t + dz \quad \text{(Equation A2)}$$

$$998 \quad Q_{in} = \sum Q_{link_{in}} + \sum Q_{runoff} + \sum Q_{external} + \sum Q_{seepage} \quad \text{(Equation A3)}$$

$$999 \quad Q_{out} = \sum Q_{link_{out}} + \sum Q_{irrigation} \quad \text{(Equation A4)}$$

1000

1001 where,  $dz$  = incremental change in stage (L);  $dt$  = computational time-step (T);  $Q_{in}$  = total  
 1002 inflow rate ( $L^3T^{-1}$ );  $Q_{out}$  = total outflow rate ( $L^3T^{-1}$ );  $A_{surface}$  = wet surface area ( $L^2$ );  $Z_{t+dt}$  =  
 1003 current water surface elevation (WSE) (L);  $Z_t$  = previous WSE (L);  $\sum Q_{link_{in}}$  = sum of all link  
 1004 flow rates entering a control volume ( $L^3T^{-1}$ );  $\sum Q_{link_{out}}$  = sum of all link flow rates leaving the  
 1005 control volume ( $L^3T^{-1}$ );  $\sum Q_{runoff}$  = sum of catchment area runoff ( $L^3T^{-1}$ );  $\sum Q_{external}$  = sum of  
 1006 all inflows from external sources such as streamflow gages ( $L^3T^{-1}$ );  $\sum Q_{seepage}$  = sum of lateral

1007 seepage inflow from groundwater model ( $L^3T^{-1}$ );  $\sum Q_{irrigation}$  = sum of water pulled out of the  
 1008 system for irrigation ( $L^3T^{-1}$ ).

1009 The overland flow along the 1D link is governed by the energy equation. The flow along  
 1010 the edges of the 2D TIN is governed by diffusive wave equation. The roughness characterization  
 1011 (Manning's  $n$ ) is governed by an exponential decay function relating Manning's  $n$  to surface depth.  
 1012 The relevant equations are given below (Equations A6-A9).

$$1013 \quad Q = \left\{ \frac{Z_1 - Z_2}{\Delta x C_f} \right\}^{1/2} \quad \text{(Equation A6)}$$

$$1014 \quad n = n_{shallow} e^{(k)(d)} \quad \text{(Equation A7)}$$

$$1015 \quad k = \frac{\ln\left(\frac{n_{deep}}{n_{shallow}}\right)}{d_{max}} \quad \text{(Equation A8)}$$

$$1016 \quad S_{f_{avg}} = \frac{4Q^2}{(K_1 + K_2)^2} \quad \text{(Equation A9)}$$

1017 where  $Q$  =flow rate ( $L^3T^{-1}$ );  $\Delta x$  =length of channel (L);  $Z_1, Z_2$ = WSE at upstream end of  
 1018 link, WSE at downstream end of link, respectively (L);  $C_f$  = conveyance factor;  $n$  = Manning's  
 1019 roughness at depth  $d$ ;  $n_{shallow}$  = Manning's roughness at ground surface;  $n_{deep}$  = Manning's  
 1020 roughness at depth =  $d_{max}$ ;  $k$  = exponential decay factor;  $d$  = depth of flow;  $d_{max}$  = user specified  
 1021 maximum depth for transitioning to  $n_{deep}$ ;  $K_1$  and  $K_2$  = channel conveyance ( $L^3T^{-1}$ ) at two cross-  
 1022 sections; and  $S_{f_{avg}}$  = average friction slope across two cross-sections.

1023 The vadose zone processes are represented through soil moisture accounting and recharge.  
 1024 ICPR uses a vertical layer method where the vadose zone (region between the ground surface and  
 1025 water table (GWT)) is divided into three vertical layers. Each layer has its own unique soil

1026 characterization which allows ICPR to account for the heterogeneity in soil properties with depth.  
 1027 Each layer is further subdivided into ten cells (total of 30 cells) to track the movement of water  
 1028 through the vadose zone. Water enters the vadose zone from the ground surface (infiltration) and  
 1029 moves in the downward direction through the cells. This movement is governed by the unsaturated  
 1030 conductivity and moisture content of each cell starting from the top cell to the bottom cell as per  
 1031 the Brooks-Corey method (Equation A10).

$$1032 \quad \frac{K(\theta)}{K_s} = \left( \frac{\theta - \theta_r}{\varphi - \theta_r} \right)^n \quad (\text{Equation A10})$$

1033 where,  $\theta$  = current moisture content;  $\theta_r$  = residual moisture content;  $\varphi$  = saturated moisture  
 1034 content;  $K(\theta)$  = unsaturated vertical conductivity at  $\theta$ ;  $K_s$  = saturated vertical conductivity;  $n =$   
 1035  $3 + \frac{2}{\lambda}$ ; and  $\lambda$  = pore size index.

1036 If the moisture content of the bottom cell exceeds its saturation capacity (saturated moisture  
 1037 content), the extra flux is delivered to the groundwater and the bottommost cell's moisture content  
 1038 is set to saturation. Next, a mass balance is performed from the bottommost cell to the topmost cell  
 1039 to update the moisture content each cell to ensure that the moisture content in the cells do not  
 1040 exceed saturation capacity. This allows fluxes to move in both direction (surface to GW and GW  
 1041 to surface) and reflects the drying or wetting of the vadose zone based on the hydraulic fluxes. If  
 1042 the GWT elevation exceeds the elevation of a cell, that cell is removed from the vadose zone and  
 1043 becomes a part of the GW. If, on the other hand, the GWT elevation decreases, additional cells  
 1044 with field capacity may be added to the vadose zone to account for the drying.

1045 The GW is represented as a TIN (2D flexible mesh) similar to the overland 2D flow. GW  
 1046 is bounded vertically by the vadose zone at the top and a bedrock layer at the bottom. The bedrock

1047 layer is assumed to be impenetrable. The movement in water is represented by a finite element  
 1048 formulation of the continuity equation depicting 2D unsteady phreatic flow (Equation A11)

$$1049 \quad n \frac{\partial h}{\partial t} = -\frac{\partial(uh)}{\partial x} - \frac{\partial(vh)}{\partial y} \quad (\text{Equation A11})$$

1050 where,  $n$  is the fillable porosity (or specific yield);  $h$  is the GW elevation (piezometric  
 1051 head);  $u$ ,  $v$  are the velocity vector components;  $t$  is time; and  $x$ ,  $y$  are the Cartesian coordinates.  
 1052 The velocity vectors for isotropic media are represented by Equation A12.

$$1053 \quad u = -K \cdot \frac{\partial h}{\partial x}; \text{ and, } v = -K \cdot \frac{\partial h}{\partial y} \quad (\text{Equation A12})$$

1054 where  $n$  is the fillable porosity (or specific yield);  $h$  is the GW elevation (piezometric head,  
 1055 L);  $u$ ,  $v$  are the velocity vector components ( $LT^{-1}$ );  $t$  is time (T). Equation A11 and A12 are solved  
 1056 simultaneously using Galerkin approximation and Green's Theorem to develop a set of partial  
 1057 differential equations. The partial differential equations are solved for six nodes of the GW TIN  
 1058 (three vertices of each triangular element and midpoint of each side of the triangle) using a  
 1059 quadratic interpolation function shown in Equation A13.

$$1060 \quad h = Ax^2 + By^2 + Cxy + Dx + Ey + F \quad (\text{Equation A13})$$

1061 where  $x$ ,  $y$  are the Cartesian coordinates (L);  $K$  is the permeability (conductivity) of the  
 1062 porous media; A – F = coefficients of the six-point quadratic function. The set of equation is solved  
 1063 using the Cholesky method and provides estimates of water transport, storage variation, and  
 1064 external flows into the vadose zone and overland flow region across the entire GW TIN. Finally,  
 1065 the seepage rates are calculated using Equation A14.

$$1066 \quad Q_{seepage} = \frac{(h_1 - h_2) \times (A) \times \phi_b}{dt_{gw}} \quad (\text{Equation A14})$$

1067            where  $Q_{seepage}$  = seepage rate ( $L^3T^{-1}$ );  $h_1$ = calculated GWT elevation (L);  $h_2$  = ground  
1068 surface elevation at node (L);  $A_{gw}$ = groundwater control volume surface area ( $L^2$ );  $\varphi_b$  = below  
1069 ground fillable porosity; and  $dt_{gw}$  = groundwater computational time increment (T).

1070

1071 **Reference**

- 1072 Afshari, S., Tavakoly, A.A., Rajib, M.A., Zheng, X., Follum, M.L., Omranian, E., Fekete, B.M., 2018.  
1073 Comparison of new generation low-complexity flood inundation mapping tools with a  
1074 hydrodynamic model. *J. Hydrol.* 556, 539–556. <https://doi.org/10.1016/j.jhydrol.2017.11.036>
- 1075 Altenau, E.H., Pavelsky, T.M., Bates, P.D., Neal, J.C., 2017. The effects of spatial resolution and  
1076 dimensionality on modeling regional-scale hydraulics in a multichannel river. *Water Resour. Res.*  
1077 53, 1683–1701. <https://doi.org/10.1002/2016WR019396>
- 1078 Banks, E.W., Simmons, C.T., Love, A.J., Shand, P., 2011. Assessing spatial and temporal connectivity  
1079 between surface water and groundwater in a regional catchment : Implications for regional scale  
1080 water quantity and quality. *J. Hydrol.* 404, 30–49. <https://doi.org/10.1016/j.jhydrol.2011.04.017>
- 1081 Baratelli, F., Flipo, N., Moatar, F., 2016. Estimation of stream-aquifer exchanges at regional scale using a  
1082 distributed model: Sensitivity to in-stream water level fluctuations, riverbed elevation and  
1083 roughness. *J. Hydrol.* 542, 686–703. <https://doi.org/10.1016/j.jhydrol.2016.09.041>
- 1084 Bhuyian, N.M., Kalyanapu, A.J., Nardi, F., 2015. Approach to Digital Elevation Model Correction by  
1085 Improving Channel Conveyance. *J. Hydrol. Eng.* 20, 1–10.  
1086 [https://doi.org/10.1061/\(ASCE\)HE.1943-5584.0001020](https://doi.org/10.1061/(ASCE)HE.1943-5584.0001020).
- 1087 Brown, R.A., Pasternack, G.B., Wallender, W.W., 2014. Synthetic river valleys: Creating prescribed  
1088 topography for form-process inquiry and river rehabilitation design. *Geomorphology* 214, 40–55.  
1089 <https://doi.org/10.1016/j.geomorph.2014.02.025>
- 1090 Brunner, P., Therrien, R., Renard, P., Simmons, C.T., Franssen, H.J.H., 2017. Advances in understanding  
1091 river-groundwater interactions. *Rev. Geophys.* 55, 818–854. <https://doi.org/10.1002/2017RG000556>
- 1092 Cardenas, M.B., Jiang, X.W., 2010. Groundwater flow, transport, and residence times through  
1093 topography-driven basins with exponentially decreasing permeability and porosity. *Water Resour.*  
1094 *Res.* <https://doi.org/10.1029/2010WR009370>
- 1095 Chow, R., Wu, H., Bennett, J.P., Dugge, J., Wöhling, T., Nowak, W., 2019. Sensitivity of Simulated  
1096 Hyporheic Exchange to River Bathymetry: The Steinlach River Test Site. *Groundwater* 57, 378–  
1097 391. <https://doi.org/10.1111/gwat.12816>
- 1098 Cienciala, P., Pasternack, G.B., 2017. Floodplain inundation response to climate, valley form, and flow  
1099 regulation on a gravel-bed river in a Mediterranean-climate region. *Geomorphology* 282, 1–17.  
1100 <https://doi.org/10.1016/j.geomorph.2017.01.006>
- 1101 Claxton, A.J., Bates, P.D., Cloke, H.L., 2003. Mixing of Hillslope, River, and Alluvial Ground Waters in  
1102 Lowland Floodplains. *Ground Water* 41, 926–936. [https://doi.org/10.1111/j.1745-  
1103 6584.2003.tb02435.x](https://doi.org/10.1111/j.1745-6584.2003.tb02435.x)
- 1104 Cook, A., Merwade, V., 2009. Effect of topographic data , geometric configuration and modeling  
1105 approach on flood inundation mapping. *J. Hydrol.* 377, 131–142.  
1106 <https://doi.org/10.1016/j.jhydrol.2009.08.015>
- 1107 Czuba, J.A., David, S.R., Edmonds, D.A., Ward, A.S., 2019. Dynamics of Surface-Water Connectivity in

- 1108 a Low-Gradient Meandering River Floodplain. *Water Resour. Res.* 55, 1849–1870.  
 1109 <https://doi.org/10.1029/2018WR023527>
- 1110 Dey, S., 2016. Role of river bathymetry in hydraulic modeling of river channels. Open Access Theses.  
 1111 Purdue University.
- 1112 Dey, S., Saksena, S., Merwade, V., 2019. Assessing the effect of different bathymetric models on  
 1113 hydraulic simulation of rivers in data sparse regions. *J. Hydrol.* 575, 838–851.  
 1114 <https://doi.org/10.1016/j.jhydrol.2019.05.085>
- 1115 Doble, R., Brunner, P., McCallum, J., Cook, P.G., 2012. An Analysis of River Bank Slope and  
 1116 Unsaturated Flow Effects on Bank Storage. *Ground Water* 50, 77–86.  
 1117 <https://doi.org/10.1111/j.1745-6584.2011.00821.x>
- 1118 Fleckenstein, J.H., Krause, S., Hannah, D.M., Boano, F., 2010. Groundwater-surface water interactions:  
 1119 New methods and models to improve understanding of processes and dynamics. *Adv. Water Resour.*  
 1120 33, 1291–1295. <https://doi.org/10.1016/j.advwatres.2010.09.011>
- 1121 Flipo, N., Mouhri, A., Labarthe, B., Biancamaria, S., Rivière, A., Weill, P., 2014. Continental  
 1122 hydrosystem modelling: the concept of nested stream-aquifer interfaces. *Hydrol. Earth Syst. Sci.* 18,  
 1123 3121–3149. <https://doi.org/10.5194/hess-18-3121-2014>
- 1124 Follum, M.L., Vera, R., Tavakoly, A.A., Gutenson, J.L., 2020. Improved accuracy and efficiency of flood  
 1125 inundation mapping of low-, medium-, and high-flow events using the AutoRoute model. *Nat.*  
 1126 *Hazards Earth Syst. Sci.* 20, 625–641. <https://doi.org/10.5194/nhess-20-625-2020>
- 1127 Gichamo, T.Z., Popescu, I., Jonoski, A., Solomatine, D., 2012. River cross-section extraction from the  
 1128 ASTER global DEM for flood modeling. *Environ. Model. Softw.* 31, 37–46.  
 1129 <https://doi.org/10.1016/j.envsoft.2011.12.003>
- 1130 Glenn, J., Tonina, D., Morehead, M.D., Fiedler, F., Benjankar, R., 2016. Effect of transect location,  
 1131 transect spacing and interpolation methods on river bathymetry accuracy. *Earth Surf. Process.*  
 1132 *Landforms* 41, 1185–1198. <https://doi.org/10.1002/esp.3891>
- 1133 Grimaldi, S., Li, Y., Walker, J.P., Pauwels, V.R.N., 2018. Effective Representation of River Geometry in  
 1134 Hydraulic Flood Forecast Models. *Water Resour. Res.* <https://doi.org/10.1002/2017WR021765>
- 1135 Grimaldi, S., Schumann, G.J.P., Shokri, A., Walker, J.P., Pauwels, V.R.N., 2019. Challenges,  
 1136 Opportunities, and Pitfalls for Global Coupled Hydrologic-Hydraulic Modeling of Floods. *Water*  
 1137 *Resour. Res.* 55, 5277–5300. <https://doi.org/10.1029/2018WR024289>
- 1138 Jung, M., Burt, T.P., Bates, P.D., 2004. Toward a conceptual model of floodplain water table response.  
 1139 *Water Resour. Res.* 40, 1–13. <https://doi.org/10.1029/2003WR002619>
- 1140 Käser, D., Graf, T., Cochand, F., McLaren, R., Therrien, R., Brunner, P., 2014. Channel Representation in  
 1141 Physically Based Models Coupling Groundwater and Surface Water: Pitfalls and How to Avoid  
 1142 Them. *Groundwater* 52, 827–836. <https://doi.org/10.1111/gwat.12143>
- 1143 Kollet, S.J., Maxwell, R.M., 2008. Capturing the influence of groundwater dynamics on land surface  
 1144 processes using an integrated, distributed watershed model. *Water Resour. Res.*  
 1145 <https://doi.org/10.1029/2007WR006004>

- 1146 Legleiter, C.J., Kyriakidis, P.C., McDonald, R.R., Nelson, J.M., 2011. Effects of uncertain topographic  
 1147 input data on two-dimensional flow modeling in a gravel-bed river. *Water Resour. Res.* 47, 1–24.  
 1148 <https://doi.org/10.1029/2010WR009618>
- 1149 Mejia, A.I., Reed, S.M., 2011. Evaluating the effects of parameterized cross section shapes and simplified  
 1150 routing with a coupled distributed hydrologic and hydraulic model. *J. Hydrol.* 409, 512–524.  
 1151 <https://doi.org/10.1016/j.jhydrol.2011.08.050>
- 1152 Merwade, V., 2004. *Geospatial Description of River Channels in Three Dimensions*. The University of  
 1153 Texas at Austin.
- 1154 Merwade, V.M., 2004. *A GIS framework for describing river channel bathymetry*. University of Texas at  
 1155 Austin.
- 1156 Merwade, V.M., Maidment, D.R., Goff, J.A., 2006. Anisotropic considerations while interpolating river  
 1157 channel bathymetry. *J. Hydrol.* 331, 731–741. <https://doi.org/10.1016/j.jhydrol.2006.06.018>
- 1158 Nash, J.E., Sutcliffe, J. V., 1970. River Flow Forecasting Through Conceptual Models Part I-A Discussion  
 1159 of Principles. *J. Hydrol.* 10, 282–290. [https://doi.org/10.1016/0022-1694\(70\)90255-6](https://doi.org/10.1016/0022-1694(70)90255-6)
- 1160 Neal, J.C., Odoni, N.A., Trigg, M.A., Freer, J.E., Garcia-Pintado, J., Mason, D.C., Wood, M., Bates, P.D.,  
 1161 2015. Efficient incorporation of channel cross-section geometry uncertainty into regional and global  
 1162 scale flood inundation models. *J. Hydrol.* 529, 169–183.  
 1163 <https://doi.org/10.1016/j.jhydrol.2015.07.026>
- 1164 Osman, Y.Z., Bruen, M.P., 2002. Modelling stream–aquifer seepage in an alluvial aquifer: an improved  
 1165 loosing-stream package for MODFLOW. *J. Hydrol.* 264, 69–86. [https://doi.org/10.1016/S0022-1694\(02\)00067-7](https://doi.org/10.1016/S0022-1694(02)00067-7)
- 1167 Price, R.K., 2009. An optimized routing model for flood forecasting. *Water Resour. Res.* 45, 1–15.  
 1168 <https://doi.org/10.1029/2008WR007103>
- 1169 Rajib, A., Liu, Z., Merwade, V., Tavakoly, A.A., Follum, M.L., 2020. Towards a large-scale locally  
 1170 relevant flood inundation modeling framework using SWAT and LISFLOOD-FP. *J. Hydrol.* 581,  
 1171 124406. <https://doi.org/10.1016/j.jhydrol.2019.124406>
- 1172 Rodríguez, E., Durand, M., Frasson, R.P. de M., 2020. Observing Rivers With Varying Spatial Scales.  
 1173 *Water Resour. Res.* 56. <https://doi.org/10.1029/2019WR026476>
- 1174 Saksena, S., Dey, S., Merwade, V., Singhofen, P.J., 2020. A Computationally Efficient and Physically  
 1175 Based Approach for Urban Flood Modeling Using a Flexible Spatiotemporal Structure. *Water*  
 1176 *Resour. Res.* 56. <https://doi.org/10.1029/2019WR025769>
- 1177 Saksena, S., Merwade, V., 2017a. Integrated Modeling of Surface-Subsurface Processes to Understand  
 1178 River-Floodplain Hydrodynamics in the Upper Wabash River Basin, in: *World Environmental and*  
 1179 *Water Resources Congress 2017*. American Society of Civil Engineers, Reston, VA, pp. 60–68.  
 1180 <https://doi.org/10.1061/9780784480595.006>
- 1181 Saksena, S., Merwade, V., 2017b. Deterministic Approach to Identify Ordinary High Water Marks Using  
 1182 Hydrologic and Hydraulic Attributes. *J. Irrig. Drain. Eng.* 143.  
 1183 [https://doi.org/10.1061/\(ASCE\)IR.1943-4774.0001148](https://doi.org/10.1061/(ASCE)IR.1943-4774.0001148)

- 1184 Saksena, S., Merwade, V., 2015. Incorporating the effect of DEM resolution and accuracy for improved  
 1185 flood inundation mapping. *J. Hydrol.* 530, 180–194. <https://doi.org/10.1016/j.jhydrol.2015.09.069>
- 1186 Saksena, S., Merwade, V., Singhofen, P.J., 2021. An Alternative Approach for Improving Prediction of  
 1187 Integrated Hydrologic-Hydraulic Models by Assessing the Impact of Intrinsic Spatial Scales Water  
 1188 Resources Research. *Water Resour. Res.* 57, 1–31. <https://doi.org/10.1029/2020WR027702>
- 1189 Saksena, S., Merwade, V., Singhofen, P.J., 2019. Flood inundation modeling and mapping by integrating  
 1190 surface and subsurface hydrology with river hydrodynamics. *J. Hydrol.* 575, 1155–1177.  
 1191 <https://doi.org/10.1016/j.jhydrol.2019.06.024>
- 1192 Saleh, F., Ducharne, A., Flipo, N., Oudin, L., Ledoux, E., 2012. Impact of river bed morphology on  
 1193 discharge and water levels simulated by a 1D Saint – Venant hydraulic model at regional scale. *J.*  
 1194 *Hydrol.* 476, 1–9. <https://doi.org/10.1016/j.jhydrol.2012.10.027>
- 1195 Schaperow, J.R., Li, D., Margulis, S.A., Lettenmaier, D.P., 2019. A Curve-Fitting Method for Estimating  
 1196 Bathymetry From Water Surface Height and Width. *Water Resour. Res.* 55, 4288–4303.  
 1197 <https://doi.org/10.1029/2019WR024938>
- 1198 Stewart, M.D., Bates, P.D., Anderson, M.G., Price, D.A., Burt, T.P., 1999. Modelling floods in  
 1199 hydrologically complex lowland river reaches. *J. Hydrol.* 223, 85–106.  
 1200 [https://doi.org/10.1016/S0022-1694\(99\)00112-2](https://doi.org/10.1016/S0022-1694(99)00112-2)
- 1201 Tijerina, D., Condon, L., FitzGerald, K., Dugger, A., O’Neill, M.M., Sampson, K., Gochis, D., Maxwell,  
 1202 R., 2021. Continental Hydrologic Intercomparison Project, Phase 1: A Large-Scale Hydrologic  
 1203 Model Comparison Over the Continental United States. *Water Resour. Res.* 57, 1–27.  
 1204 <https://doi.org/10.1029/2020WR028931>
- 1205 Tran, Q.Q., Meert, P., Huysmans, M., Willems, P., 2020. On the importance of river hydrodynamics in  
 1206 simulating groundwater levels and baseflows. *Hydrol. Process.* hyp.13667.  
 1207 <https://doi.org/10.1002/hyp.13667>
- 1208 Trigg, M.A., Wilson, M.D., Bates, P.D., Horritt, M.S., Alsdorf, D.E., Forsberg, B.R., Vega, M.C., 2009.  
 1209 Amazon flood wave hydraulics. *J. Hydrol.* 374, 92–105.  
 1210 <https://doi.org/10.1016/j.jhydrol.2009.06.004>
- 1211 Vergnes, J.-P., Habets, F., 2018. Impact of river water levels on the simulation of stream–aquifer  
 1212 exchanges over the Upper Rhine alluvial aquifer (France/Germany). *Hydrogeol. J.* 26, 2443–2457.  
 1213 <https://doi.org/10.1007/s10040-018-1788-0>
- 1214 Wing, O.E.J., Bates, P.D., Sampson, C.C., Smith, A.M., Johnson, K.A., Erickson, T.A., 2017. Validation  
 1215 of a 30 m resolution flood hazard model of the conterminous United States. *Water Resour. Res.* 53,  
 1216 7968–7986. <https://doi.org/10.1002/2017WR020917>
- 1217 Wörman, A., Packman, A.I., Marklund, L., Harvey, J.W., Stone, S.H., 2006. Exact three-dimensional  
 1218 spectral solution to surface–groundwater interactions with arbitrary surface topography. *Geophys.*  
 1219 *Res. Lett.* 33, L07402. <https://doi.org/10.1029/2006GL025747>
- 1220 Yoon, Y., Durand, M., Merry, C.J., Clark, E.A., Andreadis, K.M., Alsdorf, D.E., 2012. Estimating river  
 1221 bathymetry from data assimilation of synthetic SWOT measurements. *J. Hydrol.* 464–465, 363–375.  
 1222 <https://doi.org/10.1016/j.jhydrol.2012.07.028>

1223